PLOS ONE

RESEARCH ARTICLE

Optimised genetic algorithm-extreme learning machine approach for automatic COVID-19 detection

Musatafa Abbas Abbood Albadr[1]*, **Sabrina Tiun**[1], **Masri Ayob**[1], **Fahad Taha AL-Dhief**[2], **Khairuddin Omar**[1], **Faizal Amri Hamzah**[3]

1 CAIT, Faculty of Information Science and Technology, Universiti Kebangsaan Malaysia, Bangi, Selangor, Malaysia, **2** Department of Communication Engineering, School of Electrical Engineering, Universiti Teknologi Malaysia, UTM Johor Bahru, Johor, Malaysia, **3** Department of Emergency Medicine, Hospital Canselor Tuanku Muhriz, Universiti Kebangsaan Malaysia Medical Centre, Bandar Tun Razak, Cheras, Kuala Lumpur, Malaysia

* mustafa_abbas1988@yahoo.com

OPEN ACCESS

Citation: Albadr MAA, Tiun S, Ayob M, AL-Dhief FT, Omar K, Hamzah FA (2020) Optimised genetic algorithm-extreme learning machine approach for automatic COVID-19 detection. PLoS ONE 15(12): e0242899. https://doi.org/10.1371/journal.pone.0242899

Editor: Gulistan Raja, University of Engineering & Technology, Taxila, PAKISTAN

Received: September 17, 2020

Accepted: November 12, 2020

Published: December 15, 2020

Data Availability Statement: All image files are available from the https://www.kaggle.com/khoongweihao/covid19-xray-dataset-train-test-setsdatabase.

Funding: This project was funded by Universiti Kebangsaan Malaysia with research code GUP-2020-063.

Competing interests: NO authors have competing interests.

Abstract

The coronavirus disease (COVID-19), is an ongoing global pandemic caused by severe acute respiratory syndrome. Chest Computed Tomography (CT) is an effective method for detecting lung illnesses, including COVID-19. However, the CT scan is expensive and time-consuming. Therefore, this work focus on detecting COVID-19 using chest X-ray images because it is widely available, faster, and cheaper than CT scan. Many machine learning approaches such as Deep Learning, Neural Network, and Support Vector Machine; have used X-ray for detecting the COVID-19. Although the performance of those approaches is acceptable in terms of accuracy, however, they require high computational time and more memory space. Therefore, this work employs an Optimised Genetic Algorithm-Extreme Learning Machine (OGA-ELM) with three selection criteria (i.e., random, K-tournament, and roulette wheel) to detect COVID-19 using X-ray images. The most crucial strength factors of the Extreme Learning Machine (ELM) are: (i) high capability of the ELM in avoiding overfitting; (ii) its usability on binary and multi-type classifiers; and (iii) ELM could work as a kernel-based support vector machine with a structure of a neural network. These advantages make the ELM efficient in achieving an excellent learning performance. ELMs have successfully been applied in many domains, including medical domains such as breast cancer detection, pathological brain detection, and ductal carcinoma in situ detection, but not yet tested on detecting COVID-19. Hence, this work aims to identify the effectiveness of employing OGA-ELM in detecting COVID-19 using chest X-ray images. In order to reduce the dimensionality of a histogram oriented gradient features, we use principal component analysis. The performance of OGA-ELM is evaluated on a benchmark dataset containing 188 chest X-ray images with two classes: a healthy and a COVID-19 infected. The experimental result shows that the OGA-ELM achieves 100.00% accuracy with fast computation time. This demonstrates that OGA-ELM is an efficient method for COVID-19 detecting using chest X-ray images.

1. Introduction

Since early December 2019, the Coronavirus disease-2019 (COVID-19) had caused panic around the world. The fast escalation of COVID-19 has resulted in over twenty six millions of infections and approaching nine hundred thousand deaths globally. To date, this pandemic remains a significant challenge because it threatens human life and disrupts the economies of many countries [1, 2].

At present, the detection of viral nucleic acid utilizing real-time reverse transcriptase polymerase chain reaction (RT-PCR) is used as the standard diagnostic method. However, many hyperendemic areas or countries cannot conduct sufficient testing of RT-PCR for tens of thousands of suspected COVID-19 patients. Many efforts have been exerted to detect COVID-19 using computed tomography (CT) images for addressing the lack of reagents such as [3–5]. For example [4], conducted a chest CT for COVID-19 testing with 51 patients and achieved a high sensitivity of 98%. At the same time [5], used the technique of deep learning to detect COVID-19 utilizing CT images. Although employing CT images are useful to detect COVID-19; however, it consumes more time than X-ray imaging. The quality and quantity of CT scanners in several undeveloped regions may be low/limited, thereby leading to an inappropriate detection of COVID-19. X-ray is a well-known and broadly available technique used in diagnostic imaging and plays a vital role in epidemiological studies and clinical care [3, 6]. Numerous ambulatory care facilities have deployed X-ray imaging units (especially in rural regions) for diagnostic imaging. X-ray imaging in real-time significantly accelerates disease detection.

Given these advantages of X-ray imaging, many researchers have exerted efforts to find an accurate COVID-19 detection tool using chest X-ray images [7–9]. Researchers in [10] used artificial intelligence (AI) techniques in the early detection of COVID19 using chest X-ray images. These images were classified using several machine learning algorithms, such as support vector machine (SVM), convolutional neural network (CNN), and random forest (RF). They analyse the performance of SVM, CNN, and RF; and identified that the performance of CNN is the best among the other methods with an accuracy of 95.2% [11], used a deep learning technique for COVID-19 detection based on X-ray images. Their model consisted of three components: anomaly detection head, classification head, and backbone network. The experimental results showed that the model achieves 96.00% sensitivity. While [7], employed CNN for automatic COVID-19 detection tested on X-ray image dataset consisted of patients with COVID-19 and common pneumonia, and healthy persons to automatically detect COVID-19. They obtained 97.82% of accuracy for COVID-19 detection. In [9], the deep features of CNN were extracted and fed to the SVM for COVID-19 detection. The X-ray image datasets were collected from Open-I repository, Kaggle, and GitHub. The results showed that the accuracy of SVM and 50 layer Residual Network (ResNet50) reaches 95.38%. While the authors in [12] presented a ResNet model in their work where they considered data imbalance as one of the primary concerns. They have used 70 COVID-19 patients. The evaluation result showed 96% sensitivity, 70.7% specificity for ResNet. The work in [13] has experimented on a dataset combination of 70 COVID-19 images from one source [14] and non-COVID-19 images from Kaggle chest X-ray dataset. They proposed the Bayesian CNN model, which improves the detection rate from 85.7% to 92.9% along with the VGG16 model [15]. Further, in [16] the authors have presented a COVID-19 diagnosis system using a variant of CNN named Resnet50. The system is used 89 samples for COVID-19 infected, and 93 samples for healthy participants. The collected dataset was split into two sets like training and testing in a proportion of 80%, and 20%. The diagnosis process obtained 98.18% accuracy. In [17] the authors have developed an automated COVID-19 diagnosis system using several pre-trained models

with a small number of X-ray images. From the experimental results, it was shown that NASNetLarge performed comparatively better and achieved 98% accuracy.

On the other hand, some researchers preferred to use Extreme Learning Machine (ELM) because of its superiority over conventional SVMs [18–20] in terms of 1) its ability to prevent overfitting, 2) its usability on binary and multi-type classifiers, and 3) its kernel-based ability similar to SVM when working with a NN structure. These advantages make ELM efficient in achieving a better learning performance [18].

The distinct features of ELM, including its good generalisation, rapid training, and universal approximation/classification capability, has rendered it to be highly prominent in the AI and machine learning [21]. ELM is more suitable for single hidden layer feedforward neural networks (SLFNs) because of its excellent learning accuracy/speed, as proven in many applications [22]. ELM has better and faster generalisation performance than SVM and backpropagation-based NNs [21, 23, 24]. Besides, the effectiveness of the ELM has been proven in several medical domains such as ductal carcinoma in situ detection [25] and pathological brain detection [26, 27]. In order to further enhance the ELM [28], optimised the input-hidden layer weight and bias using Optimised Genetic Algorithm and named it as Optimised Genetic Algorithm-Extreme Learning Machine (OGA-ELM). The OGA-ELM was tested on spoken language identification and showed an excellent performance compared to ELM. However, to the best of our knowledge, no research has used ELM classifiers for detecting COVID-19 based on chest X-ray images.

Although the performance of those works was acceptable, more enhancement still needs to be done in terms of accuracy, features dimension, memory space, and computational time. The required memory space and the computational time are affected by the dimensionality of the features (number of features). The higher dimensionality requires a long computational time and large memory space [29–31]. In order to address these issues, some works have used dimensionality reduction and parallel processing techniques. Therefore, this work aims to the following contributions:

- Adapt the principal component analysis (PCA) to reduce the histogram of oriented gradients (HOG) features.
- Improve the accuracy by employing the OGA-ELM classifier to classify the chest X-ray images into healthy and COVID-19 infected.
- Evaluate the OGA-ELM performance with three selection criteria (i.e., random, K-tournament, and roulette wheel) for COVID-19 detection based on X-ray images.
- Evaluate the proposed COVID-19 detection system in terms of effectiveness and efficiency.

HOG is one of the most popular feature extraction approaches that has widely used in various image processing domains, including medical domains [32–34]. PCA is one of the most well-known schemes for dimensionality reduction [35]. This approach condenses most of the information in a dataset into a small number of dimensions.

The organisation of the paper is as follows: The proposed method (COVID-19 detection system) is provided in Section 2. Section 3 deliberates the conducted experiments and their findings. Section 4 provides general conclusions and suggestions for future research.

2. Method

2.1. General overview

The overall overview of the proposed COVID-19 detection system using the OGA–ELM approach is shown in Fig 1. The diagram illustrates various processing blocks used to create

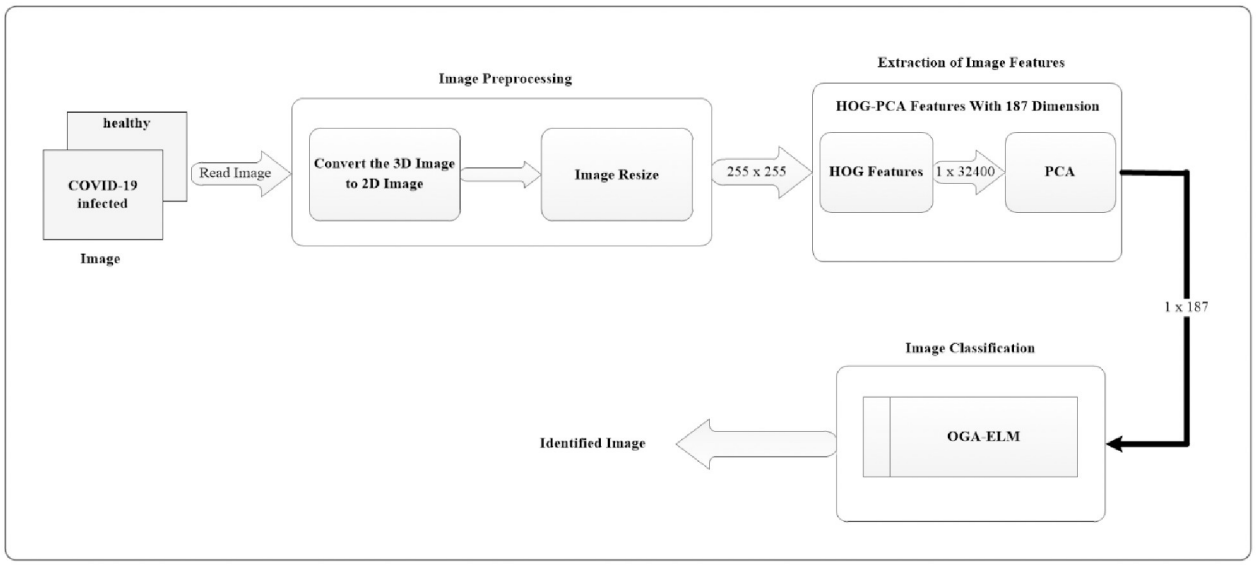

Fig 1. Illustrative block diagram of the proposed COVID-19 detection system.

https://doi.org/10.1371/journal.pone.0242899.g001

the COVID-19 detection system on chest X-ray images. The following subsections will discuss each of the processing blocks, as shown in the COVID-19 detection system (Fig 1).

2.2. Image preprocessing

The preprocessing of images consisting of two steps: image conversion and resize. The first step is to read the image and check its dimensionality. A 3D image must be converted to a 2D image. Secondly, we resize the dimensionality of the 2D image to (255 × 255). The output of this stage will be used as the input for extracting the features of the image.

2.3. Extraction of image features

At this stage, we perform two phases. Firstly, we extract the image feature using the histogram of oriented gradients (HOG) feature extraction method. HOG is a popular feature used in many image processing applications [36–38]. The HOG can be performed by dividing the image into small parts that are named cells. Each cell compiles a histogram of gradient direction for the pixel within the cell. The HOG method has four steps to extract features. The first step is calculating the gradient values to obtain the point of discrete derivative mask in the horizontal and vertical direction. The second step is the spatial orientation binning. This step has a function to give a result of a cell histogram by a voting process. Each pixel of the image within the casts a weighted vote for orientation in accordance with the closest bin in the range 0 to 180 degrees. In the third step, there is the HOG descriptor to normalize cell and histogram from the entire block region to be a vector form. The fourth step is performed by applying the block normalization. The output of the HOG feature extraction approach is a vector with a dimension of (1 × 32,400) per image and (188 × 32,400) for the entire dataset. The second phase is to apply the principal component analysis (PCA) dimensionality reduction on HOG features. PCA method has used mostly as pattern recognition system because it is very useful as the data reducing technique. The PCA processing steps can be seen in Fig 2. This step reduces the high dimensionality of the HOG features from (188 × 32,400) to (188 × 187) for

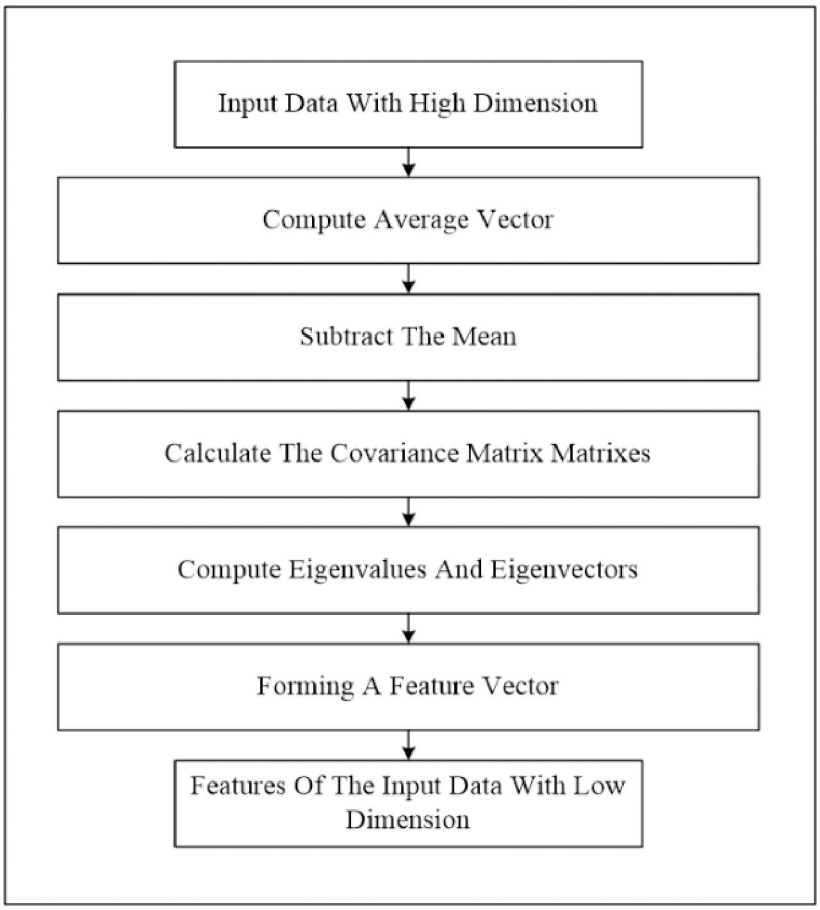

Fig 2. PCA steps.

https://doi.org/10.1371/journal.pone.0242899.g002

the entire dataset. It aims to overcome the time consumption and limited resources (requiring a large memory). The final output of feature extraction is the HOG–PCA features with (188 × 187) dimensionality for the entire dataset that will be used as input in the classification step. Fig 3 depicts the feature extraction steps in detail.

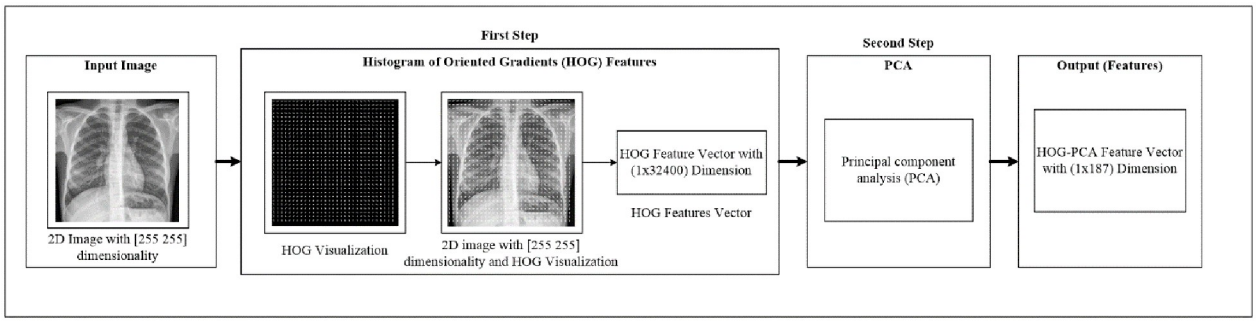

Fig 3. Feature extraction steps.

https://doi.org/10.1371/journal.pone.0242899.g003

2.4. Image classification: OGA-ELM

We adopt the OGA–ELM from [28] to classify the chest X-ray image dataset into healthy and COVID-19 infected. It utilises three selection criteria, where the input values (the weight and bias) of the hidden nodes are tuned by utilizing mutation, crossover, and selection operations. The parameters of the OGA and ELM used in the experiments are summarised in Table 1.

N is a collection of featured samples (X_i, t_i), where $X_i = [x_{i1}, x_{i2}, \ldots, x_{in}]^T \in R^n$, and $t_i = [t_{i1}, t_{i2}, \ldots, t_{im}]^T \in R^m$.

Where:

X_i is the input which is extracted features from HOG-PCA;

t_i is the true values (expected output).

At the beginning of OGA–ELM, the values of input weights, and the thresholds of hidden nodes are randomly defined and characterised as chromosomes.

$$C = \{w11,\ w12,\ \ldots,\ w1n,\ w21,\ w22,\ \ldots,\ w2n,\ wL1,\ wL2,\ \ldots,\ wLn,\ b1,\ \ldots,\ bL\}$$

Where:

w_{ij}: refers to the weight value that relates the *ith* hidden node and the *jth* input node, $w_{ij} \in [-1, 1]$;

b_i: refers to *ith* hidden node bias, $b_i \in [0, 1]$;

n: refers to the number of input node; and

L: refers to the number of hidden node.

(1+n) × L represents the chromosome dimensionality, that is, the (1+n) × L parameters that need to be optimised.

The fitness function of OGA–ELM is calculated, as shown in Eq (1) [22] to maximise the accuracy.

$$f(C) = \sqrt{\frac{\sum_j^N || \sum_k^L \rho_k g(w_k x_j + b_k) - t_j||_2^2}{N}} \tag{1}$$

Where:

ρ = matrix of the output weight;

t_j = expected output; and

N = training samples number.

Then,

$$H\rho = T \tag{2}$$

Where *T* is the expected output.

$$H = \begin{bmatrix} g(w_1.X_1 + b_1) & \cdots & g(w_L.X_1 + b_L) \\ \vdots & \cdots & \vdots \\ g(w_1.X_N + b_1) & \cdots & g(w_L.X_N + b_L) \end{bmatrix}_{N \times L} \tag{3}$$

$$\rho = \begin{bmatrix} \rho_1{}^T \\ \vdots \\ \rho_L{}^T \end{bmatrix}_{L \times m} \text{ and } T = \begin{bmatrix} t_1{}^T \\ \vdots \\ t_N{}^T \end{bmatrix}_{N \times m}$$

In [20], H indicates the NN hidden layer output matrix, and the *ith* column in *H* indicates the *ith* hidden layer nodes on the input nodes. Activation function *g* is infinitely distinguishable

Table 1. Parameters of the ELM and OGA [28].

ELM		OGA	
Parameter	**Value**	**Parameter**	**Value**
C	Combined bias and input weight	Number of iterations	100
ρ	Output weight matrix	Population size	50
Input weight	−1 to 1	Crossover	Arithmetical
Value of the biases	0–1	Mutation	Uniform
Input node numbers	Input attributes	Population of the crossover (POPC)	Refers to the crossover population, which is 70% of the population.
Hidden node numbers	(100–300), with step or increment of 25	Population of the mutation (POPM)	Refers to the mutation population, which is 30% of the population.
Output neuron	Class value	Gamma value	0.4
Activation function	Sigmoid	Tournament size	3

https://doi.org/10.1371/journal.pone.0242899.t001

when the desired number of hidden nodes is $L \leq N$. The output weights ρ can be specified by discovering the least-squares solution, as shown in the following equation:

$$\rho = H^{\dagger}T, \tag{4}$$

where $H^{\dagger}$ refers to the Moore–Penrose generalised inverse of H. Thus, the weights of output (ρ) are calculated through a mathematical transformation that avoids any long training phrase where the network parameters are iteratively tuned with several suitable learning parameters (e.g., iterations and learning rate).

First, generate the initial population (P) randomly, p = {C_1, C_2. . .C_{50}}.

Second, calculate the fitness value for each chromosome (C) of the population using Eq (1).

Third, the chromosomes are arranged based on their fitness values *f(C)*. Next, we select a pair of parents from the present population for the operation of crossover to create a pair of new children to the new population. One of the three different selection criteria will be used: random, K-tournament, and roulette wheel.

Random selection criterion refers to the process that randomly picks a chromosome from the population to be used in one of the two operations: crossover or mutation. In the random selection criterion, every single chromosome of the population has an equal chance of being chosen.

K-tournament selection criterion chooses a number of solutions (tournament size) randomly and then selects the best of the chosen solutions to be as a parent.

In the roulette wheel selection criterion, the circular wheel is separated into population size (PS) pies, where PS is the number of individuals (chromosomes) in the population. Each chromosome attains a share of the circle proportionate to its fitness value. As shown on the wheel of circumference, a selection point is picked by which the wheel is rotated. The area of the wheel landing in front of the selection point is picked as the parent. The same process is repeated for selecting the second parent. Obviously, the fitter chromosome attains a larger pie in the wheel and thus a larger chance of stopping in front of the selection point. Hence, the possibility for a chromosome to be selected is directly determined by its fitness.

Fourth, the arithmetic crossover is applied to exchange information between the two previously selected parents. The new children obtained by crossover operations are saved into the Population of the Crossover (POPC) until it reaches 70% of the population. The explanation of

the arithmetic crossover is represented by the following formulae:

$$\text{Child}_1 = \alpha.\text{x} + (1 - \alpha).\text{y} \tag{5}$$

$$\text{Child}_2 = \alpha.y + (1 - \alpha).\text{x} \tag{6}$$

Subject to the boundaries (upper bounds and lower bounds for the input-hidden layer weights [-1, 1], while for the hidden layer biases [0, 1]). In case the value of the gene has gone beyond the max (upper bound), then we make it equal to the max (upper bound). While in case the value of the gene has gone lower than the min (lower bound), then we make it equal to the min (lower bound). α is a randomly generated array with the size of the chromosome, and each value of this array is randomly generated in a range of -gamma and gamma+1 which is (-0.4, 1.4). x and y represent the first and second selected parents.

Fifth, criteria of the random selection are used to randomly choose a chromosome from the present population before implementing mutation. Mutation is applied to alter the chromosome's genes that are randomly selected. This work utilises uniform mutation. The uniform mutation works to substitute the selected gene's value with a uniform random value chosen from the gene's user-specified upper and lower bounds (for the input-hidden layer weights [-1, 1] while for the hidden layer biases [0, 1]). The new child obtained from mutation will be saved into the Population of the Mutation (POPM) until the POPM reaches 30% of the population. Fig 4 provides an example of the arithmetic crossover and uniform mutation operations.

After the selection, mutation, and crossover operations are completed, a new population is created via integrating the POPM and POPC. The following iteration will be continued along with this new population, and this process will be repeated. The iterative process could be stopped when either the results have converged or the iteration numbers is exceeded the maximum limit. OGA–ELM's pseudocode and flowchart are shown in Figs 5 and 6, respectively.

3. Experiments and results

3.1. Image dataset

This study used a dataset downloaded from [14] that contains chest X-ray images. The dataset contains two main classes: healthy and COVID-19 infected classes. The healthy class refers to the chest X-ray image of a patient negative for COVID-19 or an uninfected patient. The COVID-19 infected class refers to the X-ray image of a patient positive for COVID-19 or an infected patient. Each class of the dataset contains 94 images, and the total number of images in the entire dataset is 188. In this study, we divided the dataset to 60% for training (i.e. 56 images for each class, total is 112 images), and 40% for testing (i.e. 38 images for each class, total is 76 images). Fig 7 describes the dataset. Table 2 illustrates the dimensionality of feature extraction steps for a single image and for the entire dataset images.

3.2. Results and discussion

OGA-ELM (random, K-tournament, and roulette wheel) underwent several classification experiments based on the formulated dataset by varying the hidden neuron numbers in the range of 100–300 with an increment step of 25. Hence, the total experiment numbers for each approach was 9. Each experiment had 100 iterations. It is worth mentioning that all the experiments have been implemented in MATLAB R2019a programming language over a PC Core i7 of 3.20 GHz with 16 GB RAM and SSD 1 TB (Windows 10).

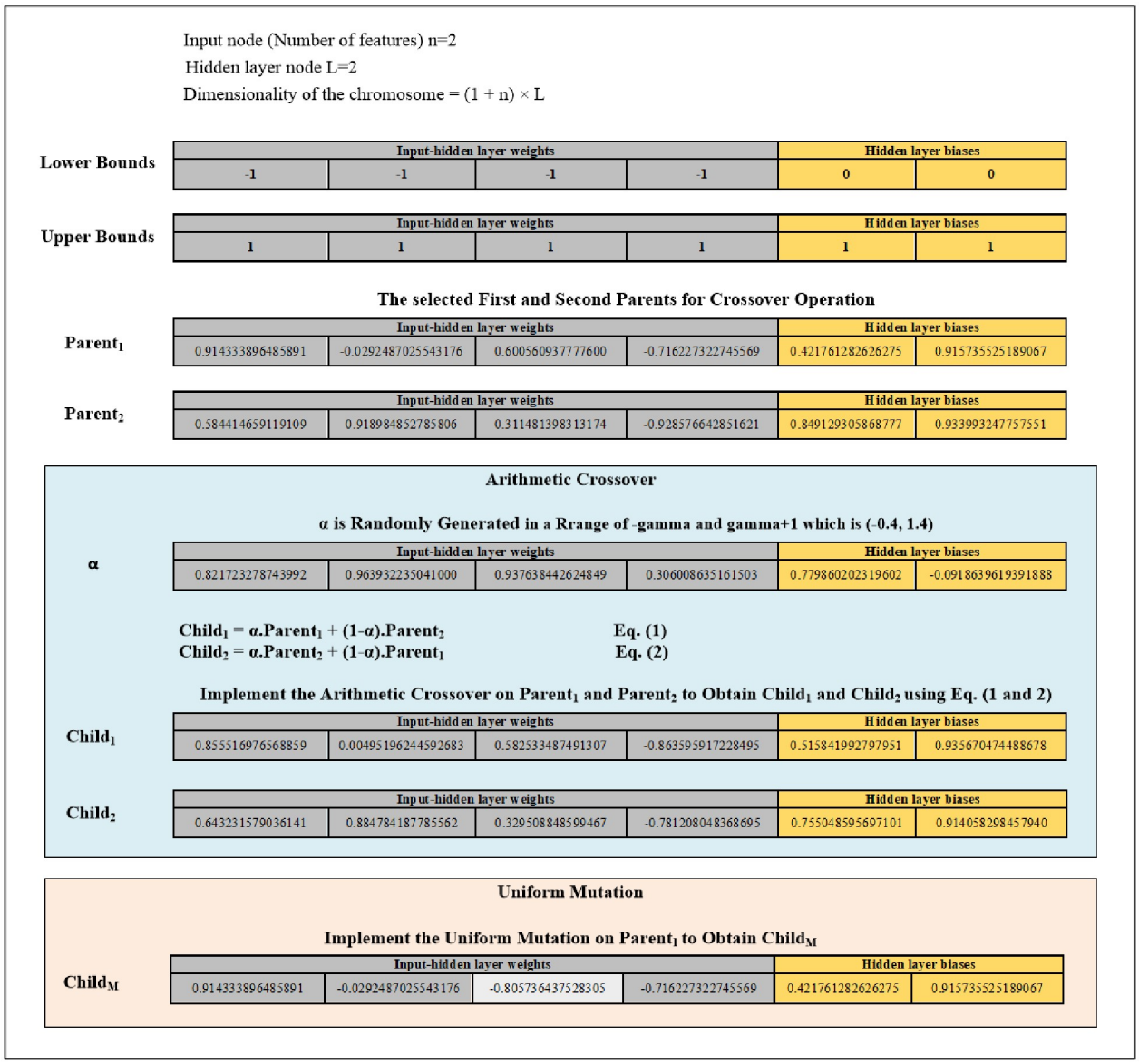

Fig 4. Diagram of the arithmetic crossover and uniform mutation operations example.

https://doi.org/10.1371/journal.pone.0242899.g004

The evaluation was based on the study in [39], where varying measures were applied. The study was selected because it tackles the issue of classifier evaluation while providing effective measures. The performance of the learning algorithms can be evaluated in several methods using supervised machine learning. A confusion matrix that has records of identified examples of each class in accordance with their correction rate was used to create the classification quality.

Hence, a number of evaluation measures were utilised in the evaluation of the three proposed approaches: OGA–ELM (random, K-tournament, and roulette wheel). The evaluation measures were based on the ground truth that requires applying the model to predict the

```
1:      Start
2:   Load the Dataset
3:   Divide the Dataset to Training set and Testing set
4:   Select the activation function and determine the hidden layer nodes L
5:      Begin the parameter optimization OGA
6:                    t ←— 1          // iteration number
7:  Initial population:  P ←— P ={C1, C2,..C50} Randomly initial the input weights and biases
8:                    Select one of the selections criteria (Roulette wheel, K-tournament and Random)
9:   Evaluation:      Train the ELM and calculate the fitness value of each variables according to Eq. (1)
10:                   While (not termination condition) do
11:                       t ←— t + 1
12:  Genetic operators:   POPC ←— {}  // initialise the crossover population
13:                       While |POPC| ≤ |70% P| do
14:                       Based on the selected "selection criteria" select a pair of parents for crossover
15:                           Mate the parents to create children C1 and C2
16:                           POPC ←— {C1, C2}
17:                       end while
18:                           POPM ←— {}  // initialise the mutation population
19:                           While |POPM| ≤ |30% P| do
20:                               randomly, select a parent for mutation
21:                               perform mutation to create a child C
22:                               POPM ←— C
23:                           end while
24:                           P ←— {POPC, POPM}     // Merge POPC and POPM to get the next genration
25:                           Train the ELM and calculate the fitness value of each variables according to Eq. (1)
26:                           Sort the P based on their fitness values.
27:                   end while
28:                   Get the optimal weights thresholds between input layer and hidden layer
29:      End the parameter optimization OGA
30:                   Calculate the output matrix H of the hidden layer Eq. (3)
31:                   Calculate the output weights ρ according to Eq. (4)
32:                   Save the predicting ELM model
33:                   The prediction results of crop evapotranspiration
34:                   Calculate the average accuracy rate
35:      End
```

Fig 5. Pseudocode of the OGA-ELM [28].

https://doi.org/10.1371/journal.pone.0242899.g005

answer in accordance with the evaluation dataset from the comparison between the actual answer and the predicted target. The measures of the evaluation were used to compare the three proposed approaches: OGA–ELM (random, K-tournament, and roulette wheel) in terms of false negative, true negative, false positive, true positive, recall, accuracy, G-mean,

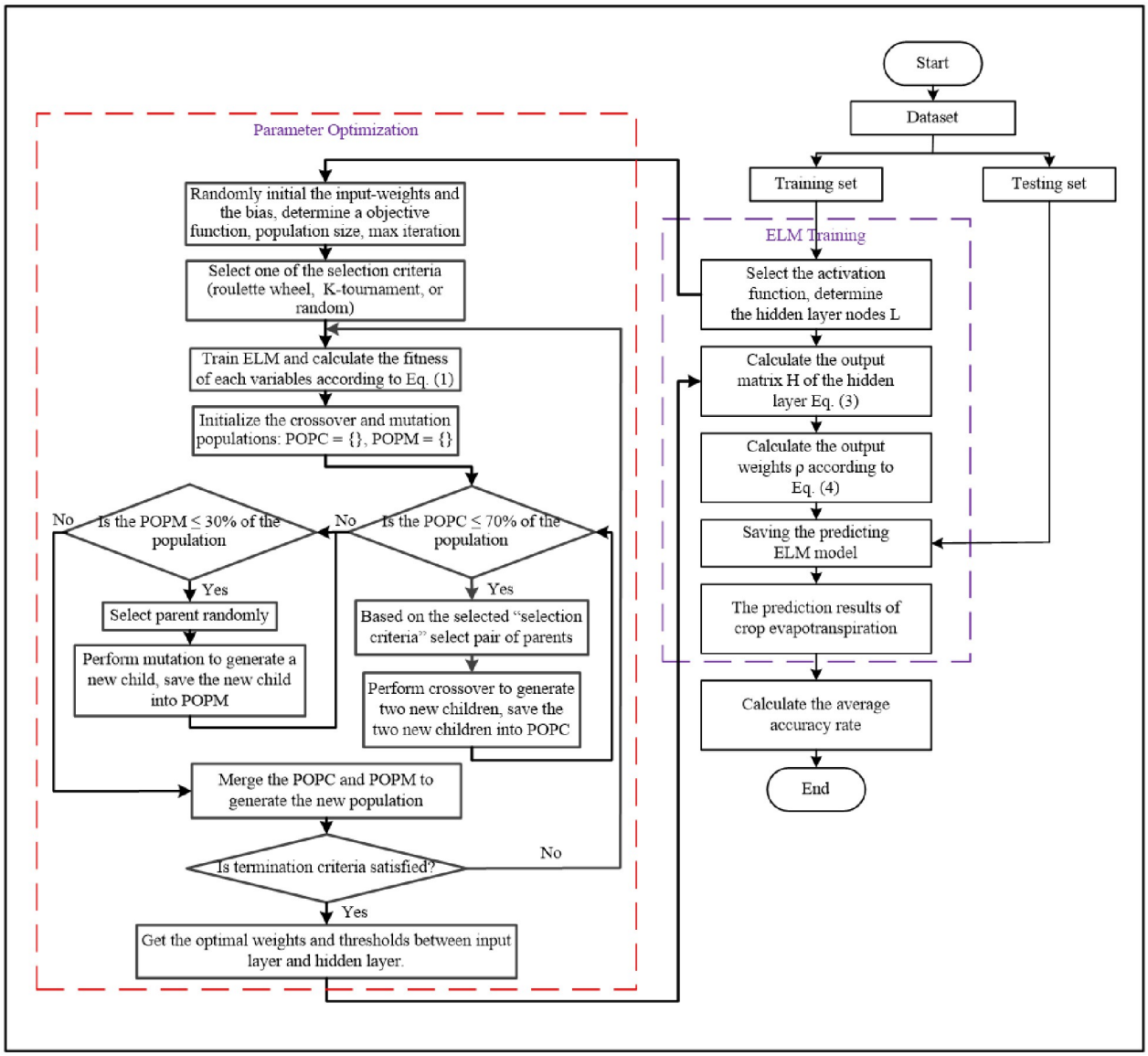

Fig 6. OGA-ELM's flowchart [28].

https://doi.org/10.1371/journal.pone.0242899.g006

Class	Number of Images	Samples of the Dataset	Class Label
Healthy	94	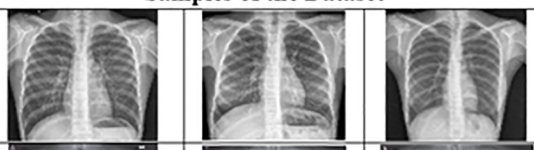	1
COVID-19 infected	94	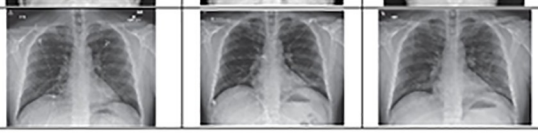	2

Fig 7. Description of the dataset.

https://doi.org/10.1371/journal.pone.0242899.g007

Table 2. Feature extraction step dimensionality for single image and entire dataset images.

Feature Extraction	Single Image Dimensionality	All Dataset Dimensionality
First Step: HOG Features	(1 × 32,400)	(188 × 23,400)
Second Step: HOG–PCA Features	(1 × 187)	(188 187)

https://doi.org/10.1371/journal.pone.0242899.t002

precision, and F-measure. Eqs (7–11) [22, 40] depict the study's evaluation measures.

$$\text{accuracy} = \frac{tp + tn}{tp + tn + fn + fp} \tag{7}$$

$$\text{precision} = \frac{tp}{tp + fp} \tag{8}$$

$$\text{recall} = \frac{tp}{tp + fn} \tag{9}$$

$$\text{F} - \text{measure} = \frac{(2 \times precision \times recall)}{(precision + recall)} \tag{10}$$

$$\text{G} - \text{Mean} = \sqrt[2]{recall \times precision} \tag{11}$$

Where *tn* indicates true negative, *tp* refers to true positive, *fn* indicates false negative, and *fp* refers to false positive.

Figs 8–16 demonstrate the comparative results between the three proposed approaches; OGA–ELM (random, K-tournament, and roulette wheel) in terms of false negative, true negative, false positive, true positive, recall, accuracy, G-mean, precision, and F-measure for all the conducted experiments. An important observation here is that the three approaches achieved

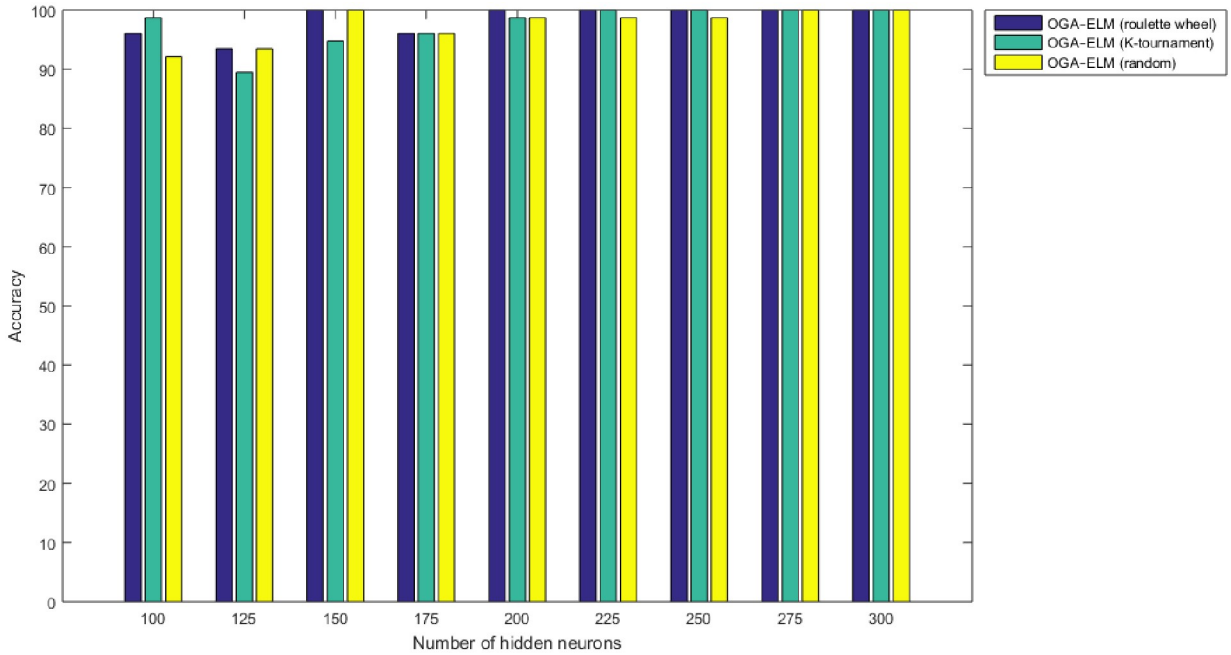

Fig 8. Accuracy results of the OGA–ELM model using random, K-tournament, and roulette wheel.

https://doi.org/10.1371/journal.pone.0242899.g008

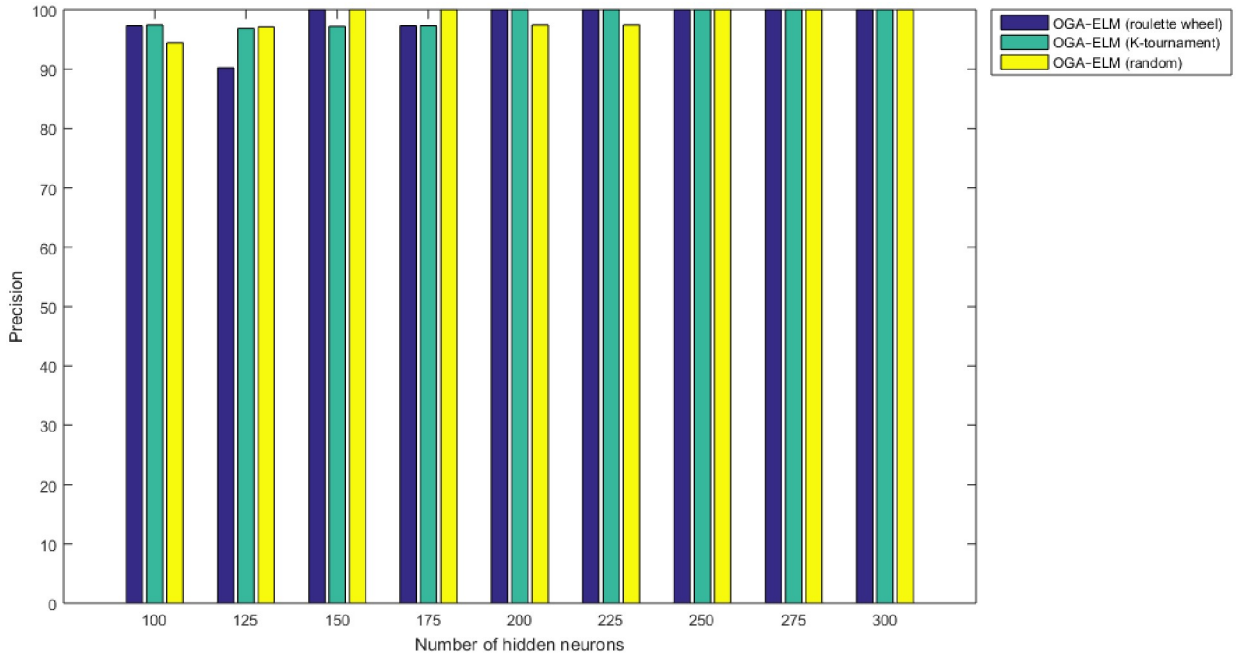

Fig 9. Precision results of the OGA–ELM model using random, K-tournament, and roulette wheel.

https://doi.org/10.1371/journal.pone.0242899.g009

the highest accuracy with various numbers of neurons, as shown in Fig 8. The achieved accuracy of the three proposed approaches: OGA–ELM (random, K-tournament, and roulette wheel) was 100.00% for OGA–ELM (K-tournament) with 225–300 neurons; OGA–ELM (roulette wheel) with 150, 200–300 neurons; and OGA–ELM (random) with 150, 275, and 300

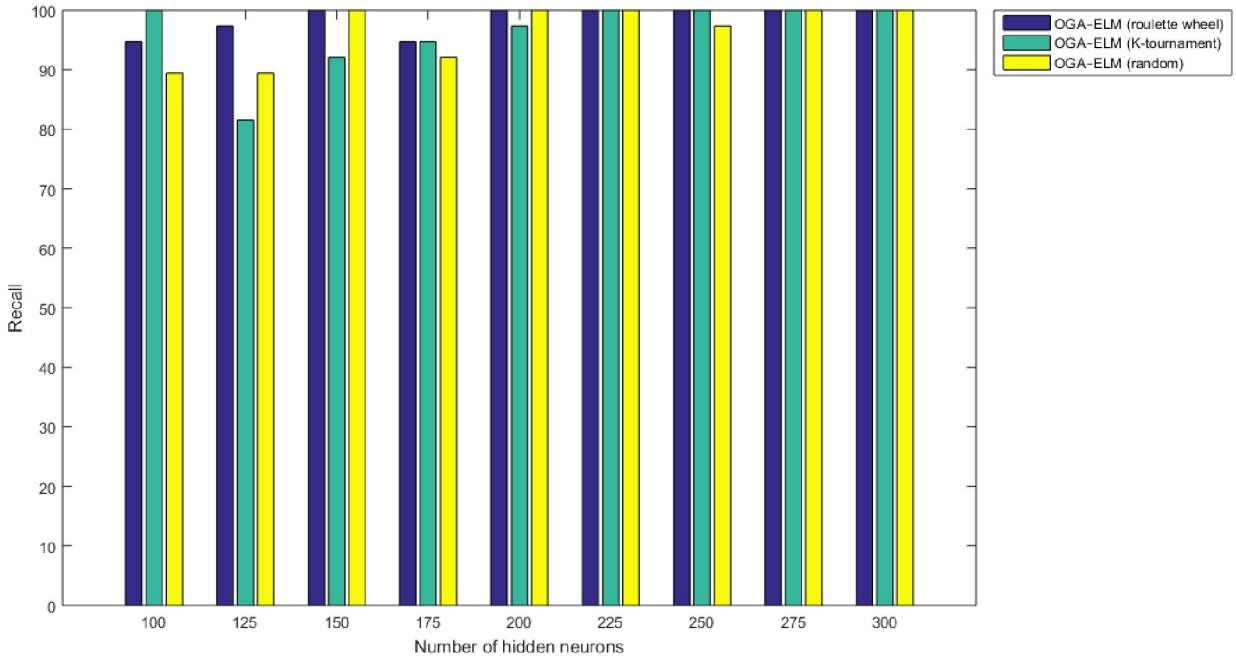

Fig 10. Recall results of the OGA–ELM model using random, K-tournament, and roulette wheel.

https://doi.org/10.1371/journal.pone.0242899.g010

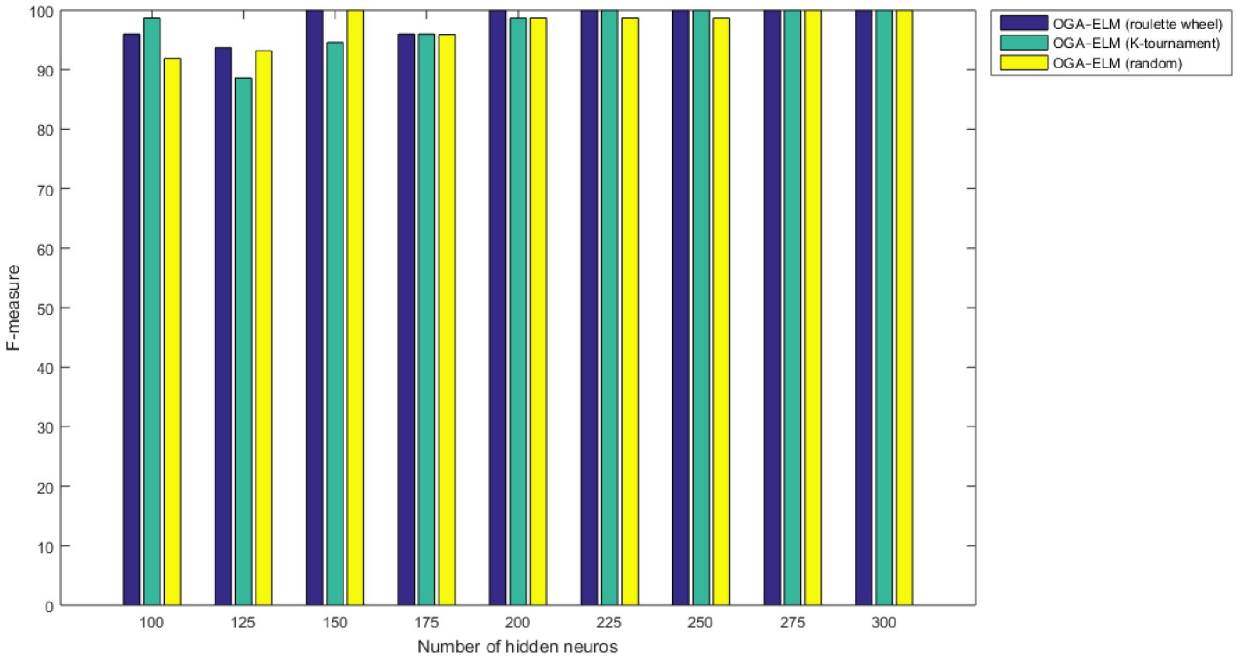

Fig 11. F-measure results of the OGA–ELM model using random, K-tournament, and roulette wheel.

https://doi.org/10.1371/journal.pone.0242899.g011

neurons. Tables 3–5 present the evaluation measures results of the OGA–ELM (random, K-tournament, and roulette wheel) through all the experiments. Furthermore, Fig 17 shows Receiver Operating Characteristic (ROC) analysis of the proposed OGA-ELM for the highest results.

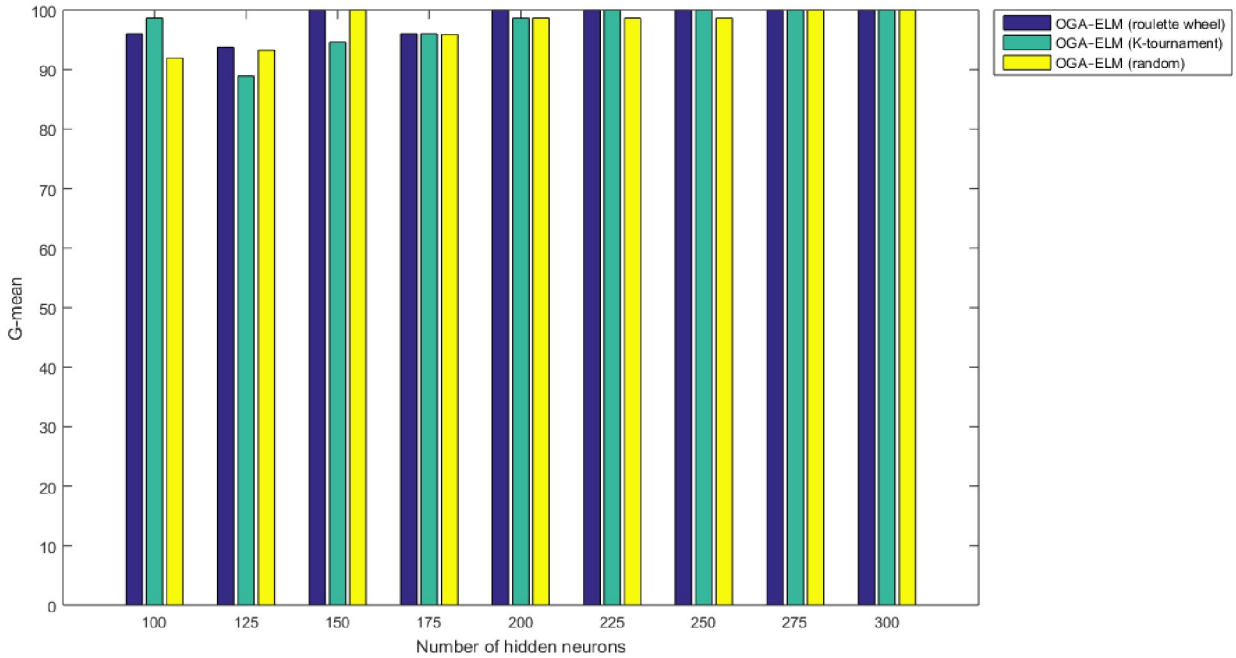

Fig 12. G-mean results of the OGA–ELM model using random, K-tournament, and roulette wheel.

https://doi.org/10.1371/journal.pone.0242899.g012

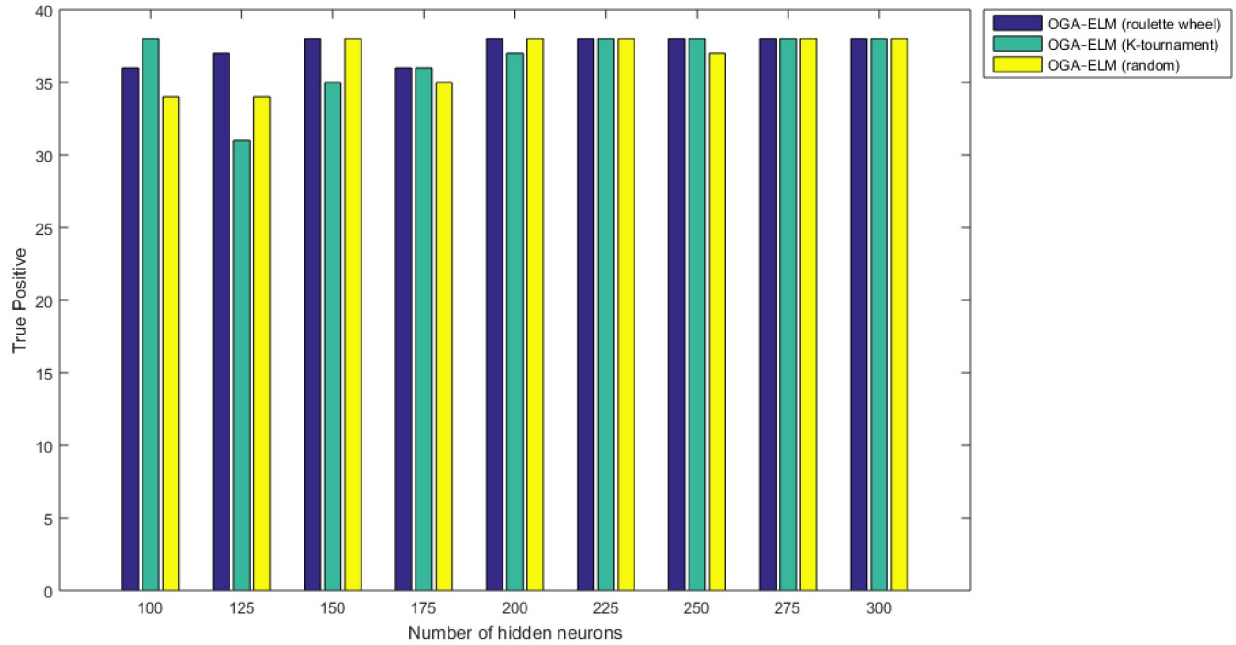

Fig 13. True positive results of the OGA–ELM model using random, K-tournament, and roulette wheel.

https://doi.org/10.1371/journal.pone.0242899.g013

A crucial observation can be concluded on the basis of the experimental results in Tables 3–5 and Figs 8–16. The OGA with three criterion selection, namely, random, K-tournament, and roulette wheel can generate appropriate biases and weights for the single hidden layer of the ELM to reduce classification errors. Avoiding inappropriate biases and weights prevents the

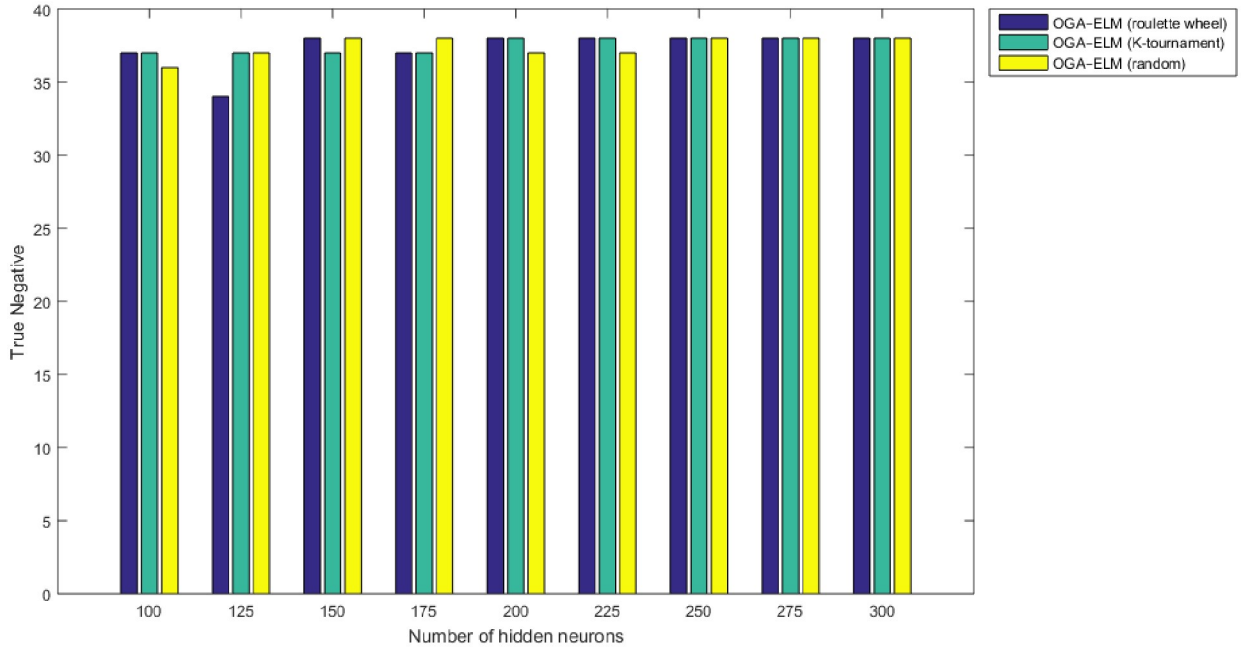

Fig 14. True negative results of the OGA–ELM model using random, K-tournament, and roulette wheel.

https://doi.org/10.1371/journal.pone.0242899.g014

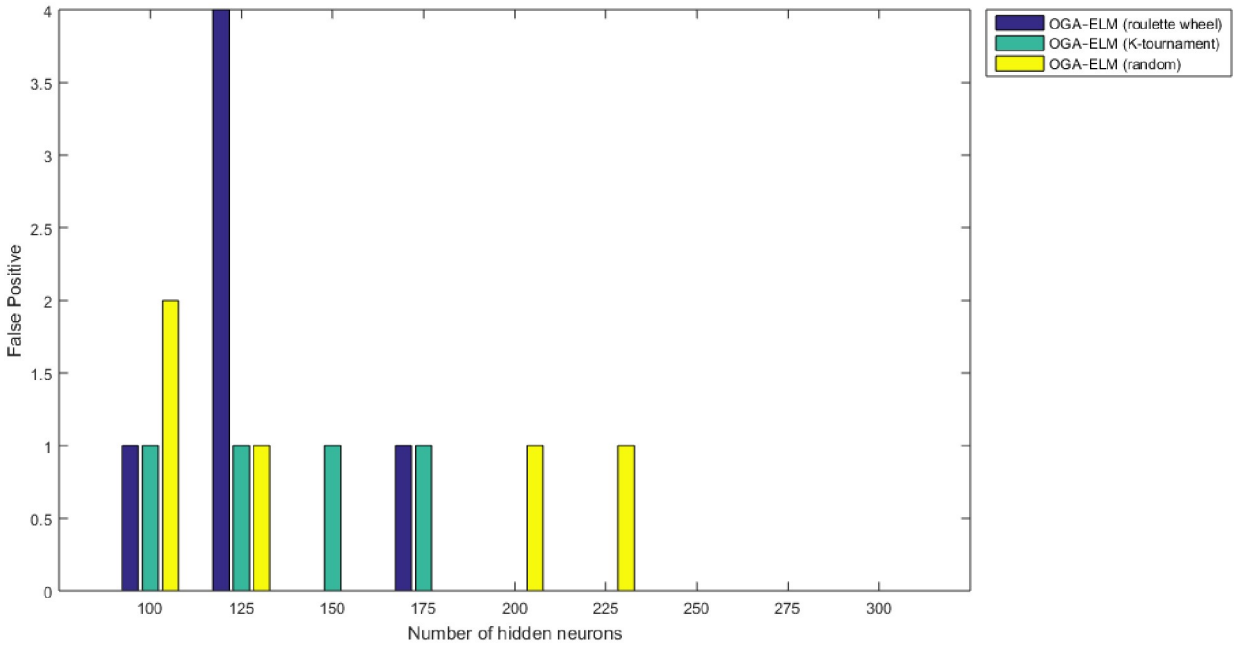

Fig 15. False positive results of the OGA–ELM model using random, K-tournament, and roulette wheel.

https://doi.org/10.1371/journal.pone.0242899.g015

ELM to be stuck in the local maxima of biases and weights. Therefore, the performance of OGA–ELM (random, K-tournament, and roulette wheel) is impressive, with an accuracy of 100.00%.

Additional experiments were conducted using the feedforward neural network (NN) as a classifier and HOG–PCA features. The NN was implemented in COVID-19 detection by

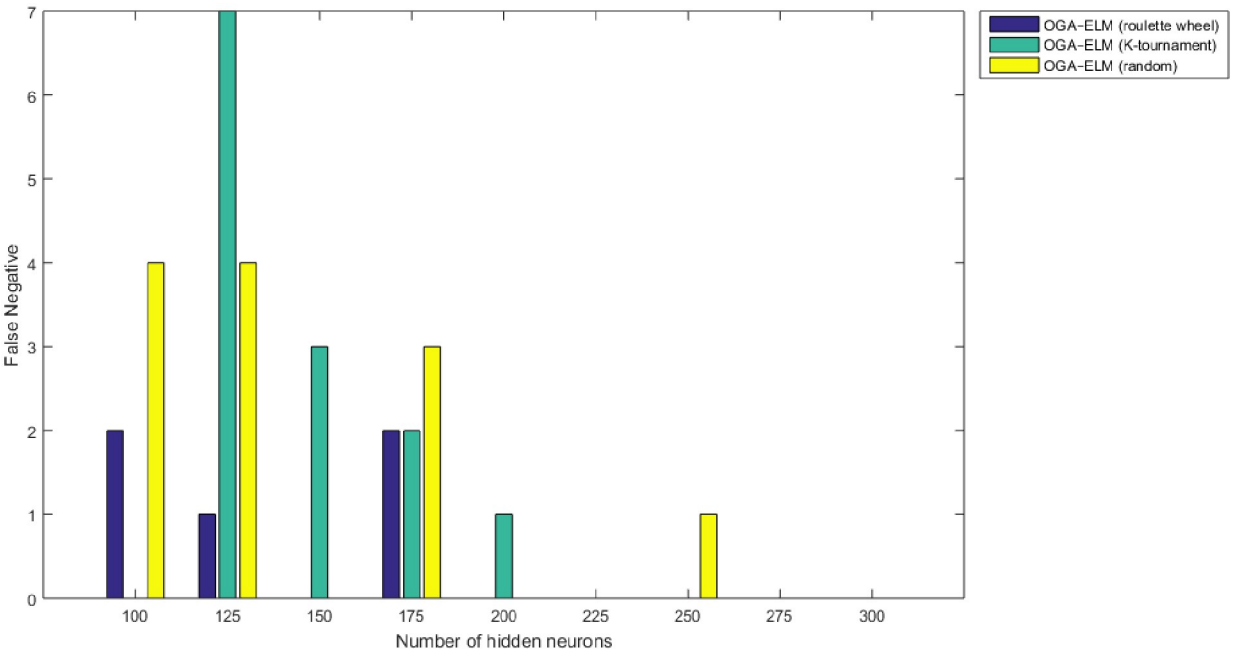

Fig 16. False negative results of the OGA–ELM model using random, K-tournament, and roulette wheel.

https://doi.org/10.1371/journal.pone.0242899.g016

Table 3. Evaluation results based on OGA–ELM (roulette wheel) model.

Number of Hidden Neurons	tp	tn	fp	fn	Accuracy	Precision	Recall	F-measure	G mean	Computational Training/Testing Time in Second
100	36	37	1	2	96.05	97.30	94.74	96.00	96.01	35.0106
125	37	34	4	1	93.42	90.24	97.37	93.67	93.74	40.2791
150	38	38	0	0	100.00	100.00	100.00	100.00	100.00	35.6772
175	36	37	1	2	96.05	97.30	94.74	96.00	96.01	40.1244
200	38	38	0	0	100.00	100.00	100.00	100.00	100.00	43.3277
225	38	38	0	0	100.00	100.00	100.00	100.00	100.00	37.9042
250	38	38	0	0	100.00	100.00	100.00	100.00	100.00	40.5361
275	38	38	0	0	100.00	100.00	100.00	100.00	100.00	48.7479
300	38	38	0	0	100.00	100.00	100.00	100.00	100.00	40.7242

Notes: where tn indicates true negative, tp refers to true positive, fn indicates false negative, and fp refers to false positive.

https://doi.org/10.1371/journal.pone.0242899.t003

Table 4. Evaluation results based on OGA–ELM (K-tournament) model.

Number of Hidden Neurons	tp	tn	fp	fn	Accuracy	Precision	Recall	F-measure	G mean	Computational Training/Testing Time in Second
100	38	37	1	0	98.68	97.44	100.00	98.70	98.71	31.4285
125	31	37	1	7	89.47	96.88	81.58	88.57	88.90	32.4359
150	35	37	1	3	94.74	97.22	92.11	94.59	94.63	32.0790
175	36	37	1	2	96.05	97.30	94.74	96.00	96.01	33.4369
200	37	38	0	1	98.68	100.00	97.37	98.67	98.68	36.0247
225	38	38	0	0	100.00	100.00	100.00	100.00	100.00	35.3846
250	38	38	0	0	100.00	100.00	100.00	100.00	100.00	36.1353
275	38	38	0	0	100.00	100.00	100.00	100.00	100.00	35.8372
300	38	38	0	0	100.00	100.00	100.00	100.00	100.00	37.1120

https://doi.org/10.1371/journal.pone.0242899.t004

varying the hidden neuron numbers in the range of 100–300 with a step of 25. NNs have been frequently used in a variety of applications with great success due to their ability to approximate complex nonlinear mappings directly from input patterns [41]. Namely, NNs do not require a user-specified problem-solving algorithm, but they could learn from existing examples, much like human beings. In addition, NNs have inherent generalization ability. This means that NNs could identify and synchronously respond to the patterns that are similar with but not identical to the ones that are employed to train NNs. It worth mention that the NN classifier has reimplemented for comparison purpose with the proposed OGA-ELM

Table 5. Evaluation results based on OGA–ELM (random) model.

Number of Hidden Neurons	tp	tn	fp	fn	Accuracy	Precision	Recall	F-measure	G mean	Computational Training/Testing Time in Second
100	34	36	2	4	92.11	94.44	89.47	91.89	91.93	28.4201
125	34	37	1	4	93.42	97.14	89.47	93.15	93.23	30.2151
150	38	38	0	0	100.00	100.00	100.00	100.00	100.00	31.4233
175	35	38	0	3	96.05	100.00	92.11	95.89	95.89	33.0367
200	38	37	1	0	98.68	97.44	100.00	98.70	98.71	33.9093
225	38	37	1	0	98.68	97.44	100.00	98.70	98.71	34.6111
250	37	38	0	1	98.68	100.00	97.37	98.67	98.68	35.3741
275	38	38	0	0	100.00	100.00	100.00	100.00	100.00	36.5370
300	38	38	0	0	100.00	100.00	100.00	100.00	100.00	36.1408

https://doi.org/10.1371/journal.pone.0242899.t005

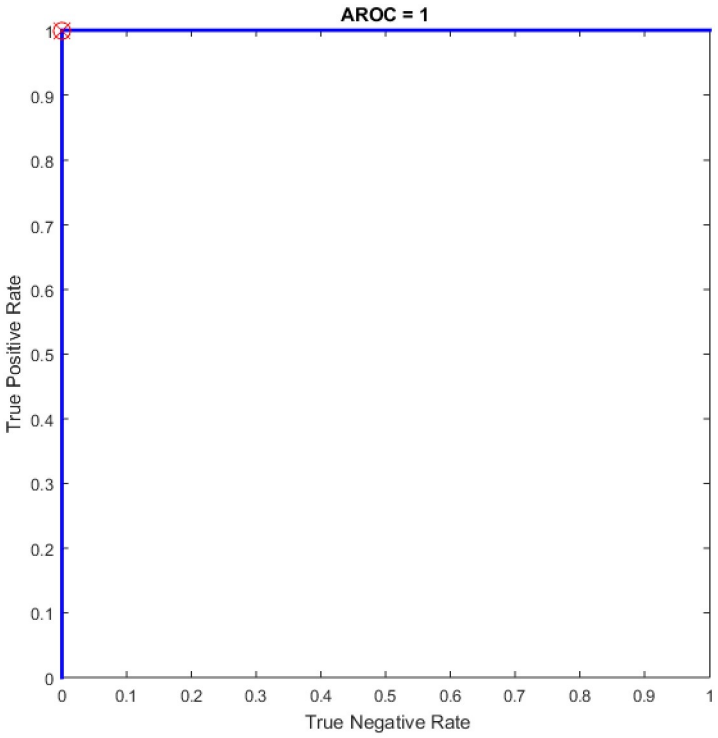

Fig 17. ROC of the OGA–ELM for the highest result.

https://doi.org/10.1371/journal.pone.0242899.g017

classifier. More details about NN can find in [42, 43]. Table 6 presents the evaluation results of the NN through in all experiments. Additionally, ROC analysis of the NN for the highest result is presented in Fig 18.

The NN is regarded as a state-of-the-art technique, and many researchers have used it in health care domains, including COVID-19 detection using chest X-ray images [8, 44–47]. Therefore, this study compared the proposed approaches of OGA–ELM (random, K-tournament, and roulette wheel) with the NN approach to evaluate the performance of OGA–ELM (random, K-tournament, and roulette wheel). As shown in the experimental results in Tables 3–6, OGA–ELM (random, K-tournament, and roulette wheel) outperforms the NN in all experiments. The accuracy of OGA–ELM (random, K-tournament, and roulette wheel) with

Table 6. Evaluation results based on NN.

Number of Hidden Neurons	tp	tn	fp	fn	Accuracy	Precision	Recall	F-measure	G-mean
100	36	38	0	2	97.37	100.00	94.74	97.30	97.33
125	36	38	0	2	97.37	100.00	94.74	97.30	97.33
150	37	38	0	1	98.68	100.00	97.37	98.67	98.68
175	37	38	0	1	98.68	100.00	97.37	98.67	98.68
200	36	38	0	2	97.37	100.00	94.74	97.30	97.33
225	37	38	0	1	98.68	100.00	97.37	98.67	98.68
250	36	38	0	2	97.37	100.00	94.74	97.30	97.33
275	36	37	1	2	96.05	97.30	94.74	96.00	96.01
300	36	38	0	2	97.37	100.00	94.74	97.30	97.33

https://doi.org/10.1371/journal.pone.0242899.t006

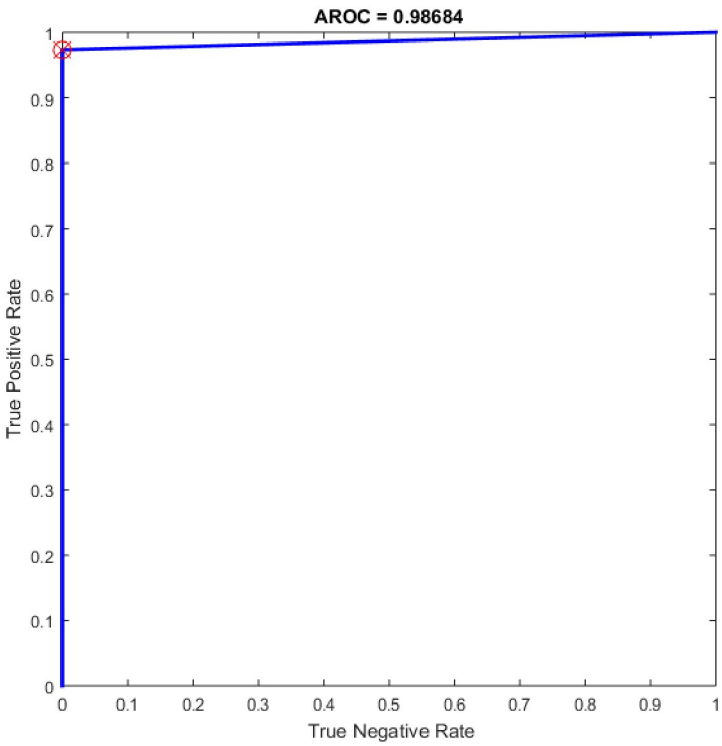

Fig 18. ROC of the NN for the highest result.

https://doi.org/10.1371/journal.pone.0242899.g018

100–300 hidden neurons is higher than that of the NN. This finding indicates that the performance results of OGA–ELM (random, K-tournament, and roulette wheel) are better than those of NN in all iterations. Tables 3–6 demonstrate the comparative results between the NN and OGA–ELM (random, K-tournament, and roulette wheel) in terms of false negative, true negative, false positive, true positive, recall, accuracy, G-mean, precision, and F-measure for all the conducted experiments. The highest accuracy was obtained by OGA-ELM (roulette wheel) with (150, 200–300) neurons, followed by OGA-ELM (K-tournament) with (225–300) neurons, OGA-ELM (random) with (150, 275, and 300) neurons, and the NN with (150, 175, and 225) neurons, as shown in Tables 3–6. The achieved accuracies were 100.00% for OGA–ELM (random, K-tournament, and roulette wheel) and 98.68% for NN. The other measures results for the NN were as follows: precision (100.00%), recall (97.37%), F-measure (98.67%), and G-mean (98.68%). The results for OGA–ELM (random, K-tournament, and roulette wheel) were as follows: precision (100.00%), recall (100.00%), F-measure (100.00%), and G-mean (100.00%).

Several experiments were performed for the basic ELM and fast learning network (FLN) with varying numbers of hidden neurons within the range of 100–300 with an increment of 25. ELM is a novel single hidden layer feedforward neural network (SLFN) where the input weights and the bias of hidden nodes are generated randomly without tuning and the output weights are determined analytically. While the FLN is based on the thought of ELM [19]. In FLN, the input weights and hidden layer biases are randomly generated, and the weight values of the connection between the output layer and the input layer and the weight values connecting the output node and the input nodes are analytically determined based on least-squares methods [48]. It worth mention that the FLN classifier has reimplemented for comparison

Table 7. Evaluation results based on basic ELM.

Number of Hidden Neurons	tp	tn	fp	fn	Accuracy	Precision	Recall	F-measure	G-mean
100	28	32	6	10	78.95	82.35	73.68	77.78	77.90
125	27	30	8	11	75.00	77.14	71.05	73.97	74.04
150	33	30	8	5	82.89	80.49	86.84	83.54	83.60
175	27	35	3	11	81.58	90.00	71.05	79.41	79.97
200	31	31	7	7	81.58	81.58	81.58	81.58	81.58
225	31	33	5	7	84.21	86.11	81.58	83.78	83.81
250	33	38	0	5	93.42	100.00	86.84	92.96	93.19
275	33	36	2	5	90.79	94.29	86.84	90.41	90.49
300	32	36	2	6	89.47	94.12	84.21	88.89	89.03

https://doi.org/10.1371/journal.pone.0242899.t007

Table 8. Evaluation results based on FLN.

Number of Hidden Neurons	tp	tn	fp	fn	Accuracy	Precision	Recall	F-measure	G-mean
100	34	38	0	4	94.74	100.00	89.47	94.44	94.59
125	33	38	0	5	93.42	100.00	86.84	92.96	93.19
150	33	38	0	5	93.42	100.00	86.84	92.96	93.19
175	32	38	0	6	92.11	100.00	84.21	91.43	91.77
200	34	38	0	4	94.74	100.00	89.47	94.44	94.59
225	33	38	0	5	93.42	100.00	86.84	92.96	93.19
250	34	38	0	4	94.74	100.00	89.47	94.44	94.59
275	35	38	0	3	96.05	100.00	92.11	95.89	95.97
300	35	38	0	3	96.05	100.00	92.11	95.89	95.97

https://doi.org/10.1371/journal.pone.0242899.t008

purpose with the proposed OGA-ELM classifier. More details about FLN can find in [48]. Tables 7 and 8 provide the experiment results of the basic ELM and FLN. The highest performance of the basic ELM was achieved with 250 neurons, and the achieved accuracy was 93.42%. The results of other evaluation measures were 92.96%, 100.00%, 86.84%, and 93.19% for F-measure, precision, recall, and G-mean, respectively. The highest performance of the FLN was achieved with 275 and 300 neurons, and the achieved accuracy was 96.05%. The results of other evaluation measures were 95.89%, 100.00%, 92.11%, and 95.97% for F-measure, precision, recall, and G-mean, respectively. Figs 19 and 20 are show the ROC of the basic ELM and FLN for the highest obtained results.

Additional experiments were conducted using SVM (linear kernel) and SVM (precomputed kernel). The term of SVM was first suggested in [49] on the foundation of statistical learning theory. It has turned into the main part of machine learning methods. It was created for binary sorting (classification). The main advantage of SVM classifier is to discover the improved decision border that exemplifies the greatest decisiveness (maximum margin) amidst the classes. The standard of SVM begins from resolving the problems of linear separable then expands to treat the non-linear cases. SVM develops a hyperplane that isolates two classes and attempts to accomplish utmost separation between the classes [50]. It worth mention that the SVM classifier has reimplemented for comparison purpose with the proposed OGA-ELM classifier. More details about SVM can find in [51, 52]. Table 9 provides the experiment results of SVM (linear kernel) and SVM (precomputed kernel). Fig 21 is show the ROC of the SVM for the highest obtained result.

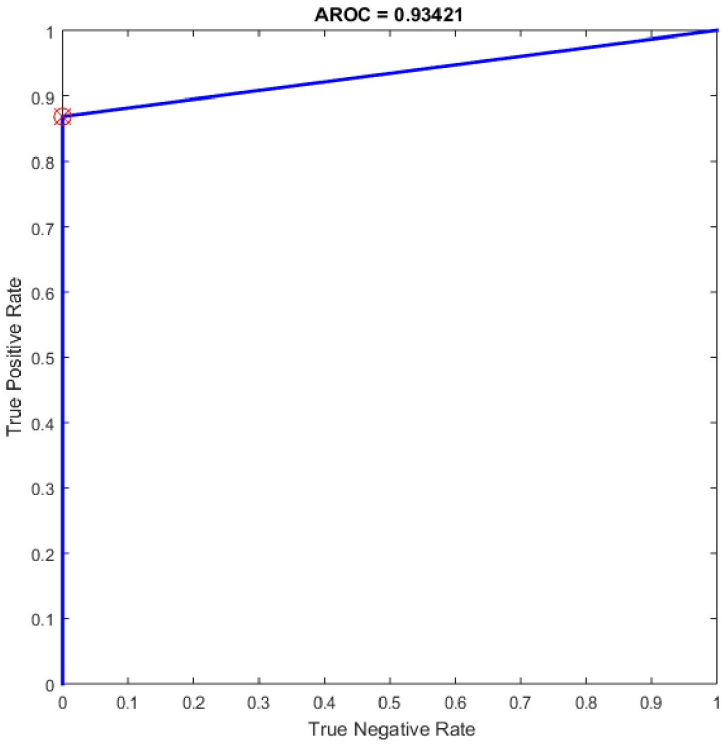

Fig 19. ROC of the ELM for the highest result.

https://doi.org/10.1371/journal.pone.0242899.g019

Furthermore, additional experiments have been conducted based on CNN in COVID-19 detection using the same dataset (see section 3.1). CNN architectures consist of two bases namely convolutional base and classifier base. The convolutional base includes three major types of layers are: a convolutional layer, an activation layer, and a pooling layer, utilized to discover the critical features of the input images, called feature maps. While the classifier base includes the dense layers that convert the feature maps to one dimension vectors to expedite the classification task using a number of neurons [53]. It worth mention that the CNN algorithm has reimplemented for comparison purpose with the proposed OGA-ELM classifier. More details about CNN can find in [54, 55]. Table 10 illustrates the CNN architecture, while Table 11 depicts the hyper-parameters of the model. The highest performance of the CNN was achieved an accuracy of 96.05%. While the results of other evaluation measures were 96.10%, 94.87%, 97.37%, and 96.11% for F-measure, precision, recall, and G-mean, respectively. The ROC of CNN for the highest result is show in Fig 22.

As the results shown in Tables 3–9 and 12, the performance of OGA–ELM (random, K-tournament, and roulette wheel) outperformed the NN, basic ELM, FLN, SVM, and CNN in all experiments. Therefore, the performance of OGA–ELM (random, K-tournament, and roulette wheel) was very impressive, with an accuracy of 100.00%. Besides, Fig 23 shows the comparison of the highest achieved accuracies for OGA-ELM, NN, basic ELM, FLN, SVM, and CNN.

In addition, the proposed method has fast computation time in all experiments with only a few seconds for detection. This study confirms the combination of the HOG-PCA features with OGA–ELM classifier is an efficient system for COVID-19 detection using chest X-ray images that could help doctors in easily detecting COVID-19 in clinical practice. Furthermore,

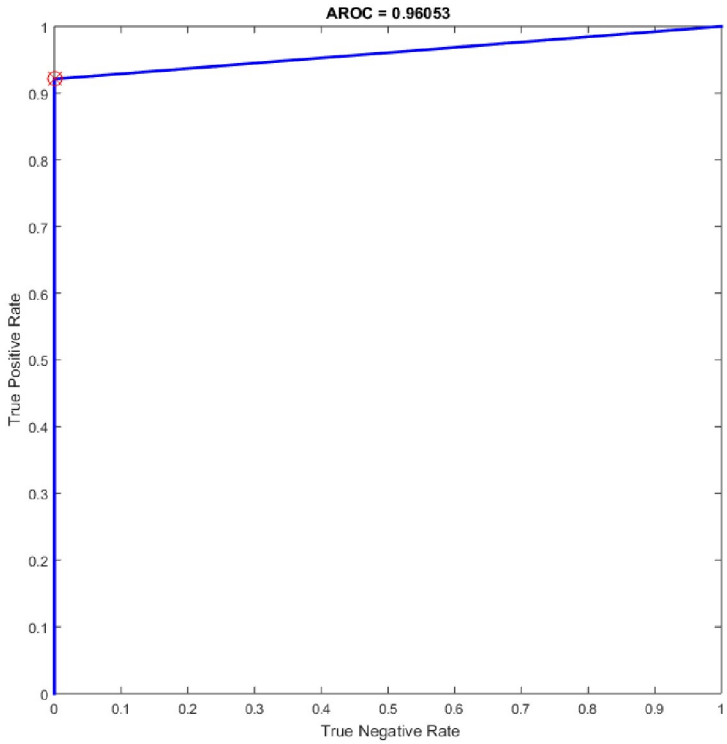

Fig 20. ROC of the FLN for the highest result.

https://doi.org/10.1371/journal.pone.0242899.g020

Table 9. Evaluation results based on SVM.

	tp	tn	fp	fn	Accuracy	Precision	Recall	F-measure	G-mean
SVM (linear kernel)	31	38	0	7	90.79	100.00	81.58	89.86	90.32
SVM (precomputed kernel)	35	38	0	3	96.05	100.00	92.11	95.89	95.97

https://doi.org/10.1371/journal.pone.0242899.t009

in order to evaluate the proposed OGA-ELM in the detection of COVID-19, Table 13 shows the comparison of accuracy between our method with other recent methods in [9, 56–60] which are worked on the detection of COVID-19 using deep learning and machine learning algorithms.

Based on Table 13, it shows that the proposed OGA-ELM method has outperformed all methods in terms of accuracy for COVID-19 detection. However, this work has some limitations that can be summarized as follow:

- The images dataset that used for training and testing are small.
- The proposed method has focused on classifying images into two classes only, healthy or COVID-19, and ignoring other lung diseases.

4. Conclusion

We have proposed the histogram oriented gradient-principal component analysis (HOG-PCA) features and optimised genetic algorithm-extreme learning machine (OGA-ELM) (with

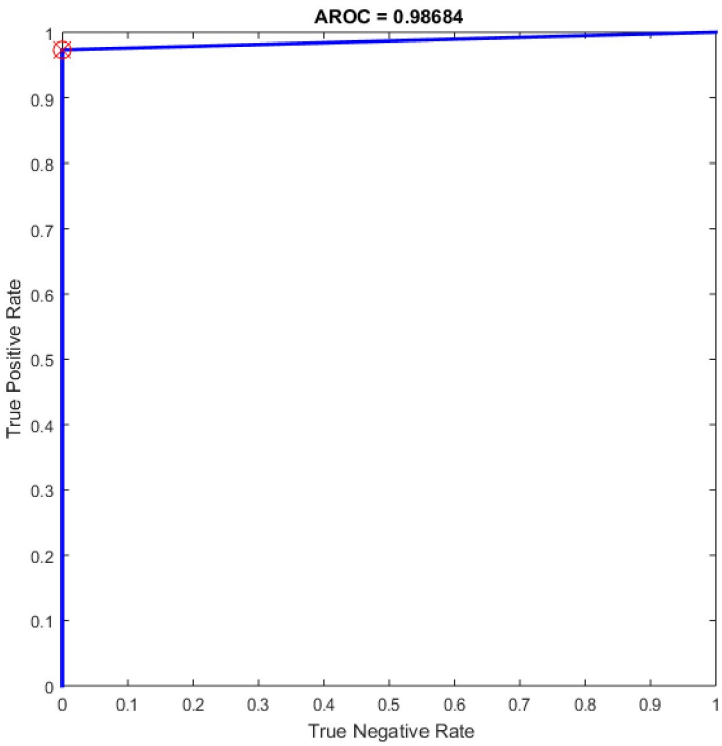

Fig 21. ROC of the SVM for the highest result.

https://doi.org/10.1371/journal.pone.0242899.g021

random, K-tournament, and roulette wheel selection mechanism) approaches using chest X-ray images, to detect COVID-19 disease efficiently. We used a benchmark dataset of chest X-ray images that were collected from COVID-19 patients and healthy people to evaluate the efficacy of the proposed method. Results showed that the OGA–ELM (random, K-tournament,

Table 10. The CNN architecture factors.

Layer Name	CNN
Input Image	128x128x1 images with 'zerocenter' normalization
Convolution	8 3x3 convolutions with stride [1 1] and padding 'same'
Batch Normalisation	Batch normalisation
Activation Function	ReLU
Max Pooling	2x2 max pooling with stride [2 2] and padding [0 0 0 0]
Convolution	16 3x3 convolutions with stride [1 1] and padding 'same'
Batch Normalisation	Batch normalisation
Activation Function	ReLU
Max Pooling	2x2 max pooling with stride [2 2] and padding [0 0 0 0]
Convolution	32 3x3 convolutions with stride [1 1] and padding 'same'
Batch Normalisation	Batch normalisation
Activation Function	ReLU
Fully Connected	2 fully connected layer
Softmax	softmax
Output Classification	crossentropyex

https://doi.org/10.1371/journal.pone.0242899.t010

Table 11. The trained model parameters used in COVID-19 detection.

Hyper-Parameters	Values
Optimisation Method	SGDM
Rate of Learning	0.01
Max Epochs	4
Shuffle	every-epoch
Frequency Validation	30
Momentum	0.90
Batch Size	128

https://doi.org/10.1371/journal.pone.0242899.t011

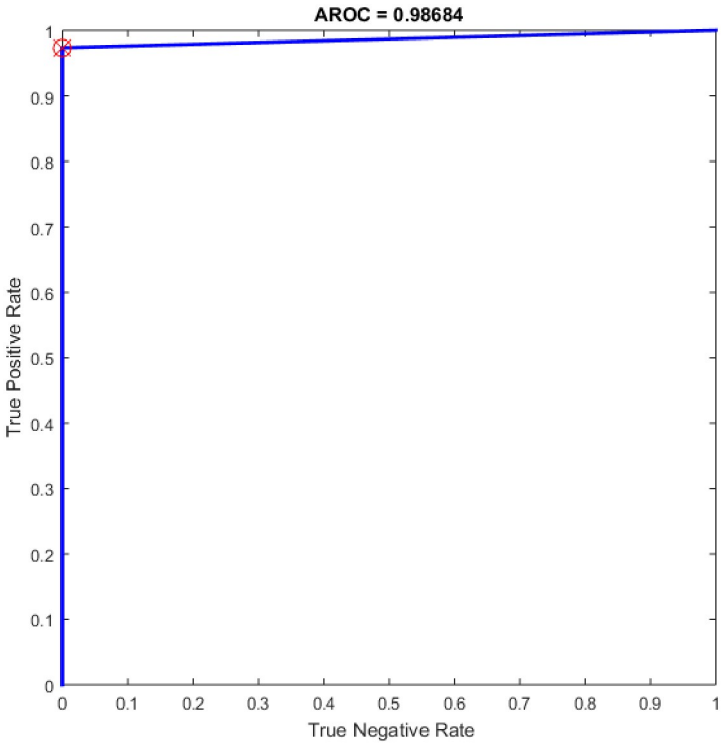

Fig 22. ROC of the CNN for the highest result.

https://doi.org/10.1371/journal.pone.0242899.g022

Table 12. Evaluation results based on CNN.

	tp	tn	fp	fn	Accuracy	Precision	Recall	F-measure	G-mean
CNN	37	36	2	1	96.05	94.87	97.37	96.10	96.11

https://doi.org/10.1371/journal.pone.0242899.t012

and roulette wheel) exhibit remarkable performance and achieves 100.00% accuracy. In addition, no machine learning was expected to perform 100% accurately but only be achieved by managing data. This demonstrated that the OGA-ELM had improved the effectiveness (accuracy) of the automatic COVID-19 detection compared to neural network (NN), basic extreme learning machine (ELM), fast learning network (FLN), support vector machine (SVM), and convolutional neural network (CNN). Indeed, the HOG-PCA features with low dimensionality had enhanced the efficiency (computational time), and required less memory space, where the low dimensionally lead to speed up the classification process and requires low memory space.

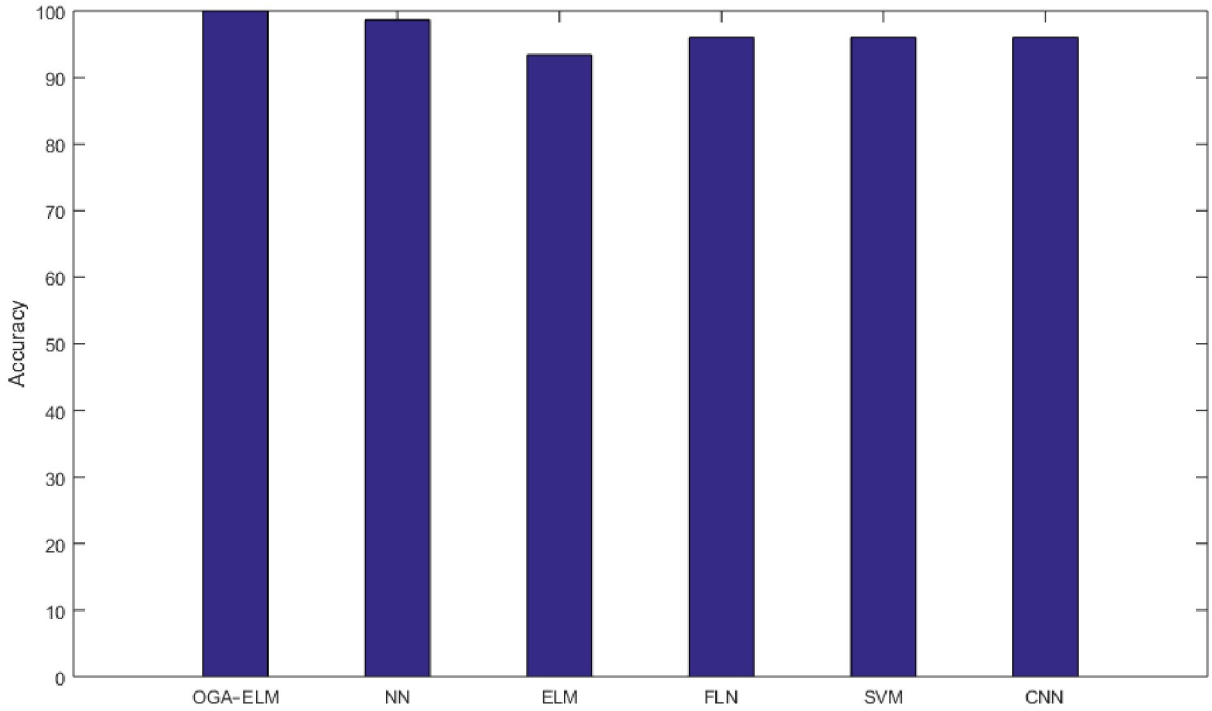

Fig 23. The highest achieved accuracy for all methods.

https://doi.org/10.1371/journal.pone.0242899.g023

Table 13. Comparison of accuracies between methods.

Methods	Accuracy
Our Method (OGA-ELM)	100.00%
Method in [58]	97.48%
Method in [56]	95.12%
Method in [57]	98%
Method in [60]	94.1%
Method in [9]	95.38%
Method in [59]	90%

https://doi.org/10.1371/journal.pone.0242899.t013

This work provides insights into the application of HOG–PCA features with OGA–ELM (random, K-tournament, and roulette wheel) to detect COVID-19 in early stage. In future research, the classification performance of the OGA–ELM (random, K-tournament, and roulette wheel) models based on HOG–PCA features can be tested on a dataset with a high number of images. In addition, another future research can include using the OGA-ELM in other healthcare applications.

Author Contributions

Conceptualization: Musatafa Abbas Abbood Albadr.

Data curation: Musatafa Abbas Abbood Albadr.

Formal analysis: Musatafa Abbas Abbood Albadr.

Funding acquisition: Sabrina Tiun.

Investigation: Musatafa Abbas Abbood Albadr, Fahad Taha AL-Dhief.

Methodology: Musatafa Abbas Abbood Albadr.

Project administration: Sabrina Tiun.

Software: Musatafa Abbas Abbood Albadr.

Supervision: Sabrina Tiun, Masri Ayob.

Validation: Musatafa Abbas Abbood Albadr.

Visualization: Musatafa Abbas Abbood Albadr, Faizal Amri Hamzah.

Writing – original draft: Musatafa Abbas Abbood Albadr.

Writing – review & editing: Musatafa Abbas Abbood Albadr, Fahad Taha AL-Dhief, Khairuddin Omar, Faizal Amri Hamzah.

References

1. Bai Y, Yao L, Wei T, Tian F, Jin D-Y, Chen L, et al. (2020) Presumed asymptomatic carrier transmission of COVID-19. Jama 323: 1406–1407. https://doi.org/10.1001/jama.2020.2565 PMID: 32083643
2. Chen H, Guo J, Wang C, Luo F, Yu X, Zhang W, et al. (2020) Clinical characteristics and intrauterine vertical transmission potential of COVID-19 infection in nine pregnant women: a retrospective review of medical records. The Lancet 395: 809–815. https://doi.org/10.1016/S0140-6736(20)30360-3 PMID: 32151335
3. Cherian T, Mulholland EK, Carlin JB, Ostensen H, Amin R, Campo Md, et al. (2005) Standardized interpretation of paediatric chest radiographs for the diagnosis of pneumonia in epidemiological studies. Bulletin of the World Health Organization 83: 353–359. PMID: 15976876
4. Fang Y, Zhang H, Xie J, Lin M, Ying L, Pang P, et al. (2020) Sensitivity of chest CT for COVID-19: comparison to RT-PCR. Radiology: 200432. https://doi.org/10.1148/radiol.2020200432 PMID: 32073353
5. Gozes O, Frid-Adar M, Greenspan H, Browning PD, Zhang H, Ji W, et al. (2020) Rapid ai development cycle for the coronavirus (covid-19) pandemic: Initial results for automated detection & patient monitoring using deep learning ct image analysis. arXiv preprint arXiv:200305037.
6. Franquet T (2001) Imaging of pneumonia: trends and algorithms. European Respiratory Journal 18: 196–208. https://doi.org/10.1183/09031936.01.00213501 PMID: 11510793
7. Apostolopoulos ID, Mpesiana TA (2020) Covid-19: automatic detection from x-ray images utilizing transfer learning with convolutional neural networks. Physical and Engineering Sciences in Medicine: 1. https://doi.org/10.1007/s13246-020-00865-4 PMID: 32524445
8. Narin A, Kaya C, Pamuk Z (2020) Automatic detection of coronavirus disease (covid-19) using x-ray images and deep convolutional neural networks. arXiv preprint arXiv:200310849.
9. Sethy PK, Behera SK (2020) Detection of coronavirus disease (covid-19) based on deep features. Preprints 2020030300: 2020.
10. Alqudah AM, Qazan S, Alquran H, Qasmieh IA, Alqudah A (2020) COVID-19 Detection from X-ray Images Using Different Artificial Intelligence Hybrid Models. Jordan Journal of Electrical Engineering 6: 168.
11. Zhang J, Xie Y, Liao Z, Pang G, Verjans J, Li W, et al. (2020) Viral pneumonia screening on chest X-ray images using confidence-aware anomaly detection. arXiv: 200312338.
12. Zhang J, Xie Y, Li Y, Shen C, Xia Y (2020) Covid-19 screening on chest x-ray images using deep learning based anomaly detection. arXiv preprint arXiv:200312338.
13. Ghoshal B, Tucker A (2020) Estimating uncertainty and interpretability in deep learning for coronavirus (COVID-19) detection. arXiv preprint arXiv:200310769.
14. Cohen JP, Morrison P, Dao L, Roth K, Duong TQ, Ghassemi M (2020) Covid-19 image data collection: Prospective predictions are the future. arXiv preprint arXiv:200611988.
15. Shi F, Wang J, Shi J, Wu Z, Wang Q, Tang Z, et al. (2020) Review of artificial intelligence techniques in imaging data acquisition, segmentation and diagnosis for covid-19. IEEE reviews in biomedical engineering. https://doi.org/10.1109/RBME.2020.2987975 PMID: 32305937

16. Bukhari SUK, Bukhari SSK, Syed A, SHAH SSH (2020) The diagnostic evaluation of Convolutional Neural Network (CNN) for the assessment of chest X-ray of patients infected with COVID-19. medRxiv.

17. Punn NS, Agarwal S (2020) Automated diagnosis of COVID-19 with limited posteroanterior chest X-ray images using fine-tuned deep neural networks. arXiv preprint arXiv:200411676.

18. Albadr MAA, Tiun S (2020) Spoken Language Identification Based on Particle Swarm Optimisation–Extreme Learning Machine Approach. Circuits, Systems, and Signal Processing: 1–27.

19. Albadra MAA, Tiuna S (2017) Extreme learning machine: a review. International Journal of Applied Engineering Research 12: 4610–4623.

20. Huang G-B, Zhu Q-Y, Siew C-K (2006) Extreme learning machine: theory and applications. Neurocomputing 70: 489–501.

21. Huang G-B, Zhou H, Ding X, Zhang R (2011) Extreme learning machine for regression and multiclass classification. IEEE Transactions on Systems, Man, and Cybernetics, Part B (Cybernetics) 42: 513–529. https://doi.org/10.1109/TSMCB.2011.2168604 PMID: 21984515

22. Albadr MAA, Tiun S, AL-Dhief FT, Sammour MA (2018) Spoken language identification based on the enhanced self-adjusting extreme learning machine approach. PloS one 13: e0194770. https://doi.org/10.1371/journal.pone.0194770 PMID: 29672546

23. Huang G-B (2014) An insight into extreme learning machines: random neurons, random features and kernels. Cognitive Computation 6: 376–390.

24. Huang G-B, Chen L, Siew CK (2006) Universal approximation using incremental constructive feedforward networks with random hidden nodes. IEEE Trans Neural Networks 17: 879–892. https://doi.org/10.1109/TNN.2006.875977 PMID: 16856652

25. Wang S-H, Muhammad K, Phillips P, Dong Z, Zhang Y-D (2017) Ductal carcinoma in situ detection in breast thermography by extreme learning machine and combination of statistical measure and fractal dimension. Journal of Ambient Intelligence and Humanized Computing: 1–11.

26. Lu S, Lu Z, Phillips P, Wang S, Zhang Y (2018) Pathological brain detection in magnetic resonance imaging using combined features and improved extreme learning machines. Journal of Medical Imaging and Health Informatics 8: 1486–1490.

27. Zhang Y-D, Zhao G, Sun J, Wu X, Wang Z-H, Liu H-M, et al. (2018) Smart pathological brain detection by synthetic minority oversampling technique, extreme learning machine, and Jaya algorithm. Multimedia Tools and Applications 77: 22629–22648.

28. Albadr MAA, Tiun S, Ayob M, AL-Dhief FT (2019) Spoken language identification based on optimised genetic algorithm–extreme learning machine approach. International Journal of Speech Technology 22: 711–727.

29. Mu Y, Liu X, Wang L (2018) A Pearson's correlation coefficient based decision tree and its parallel implementation. Information Sciences 435: 40–58.

30. Xu M, Li T, Wang Z, Deng X, Yang R, Guan Z (2018) Reducing complexity of HEVC: A deep learning approach. IEEE Transactions on Image Processing 27: 5044–5059. https://doi.org/10.1109/TIP.2018.2847035 PMID: 29994256

31. Yu T, Zhang J, Cai W, Qi F (2018) Toward real-time volumetric tomography for combustion diagnostics via dimension reduction. Optics letters 43: 1107–1110. https://doi.org/10.1364/OL.43.001107 PMID: 29489791

32. Abdel-Nasser M, Moreno A, Puig D (2019) Breast cancer detection in thermal infrared images using representation learning and texture analysis methods. Electronics 8: 100.

33. Abdel-Nasser M, Saleh A, Moreno A, Puig D (2016) Automatic nipple detection in breast thermograms. Expert Systems with Applications 64: 365–374.

34. Dalal N, Triggs B. Histograms of oriented gradients for human detection; 2005. IEEE. pp. 886–893.

35. Marsboom C, Vrebos D, Staes J, Meire P (2018) Using dimension reduction PCA to identify ecosystem service bundles. Ecological Indicators 87: 209–260.

36. Quoc Bao T, Tan Kiet NT, Quoc Dinh T, Hiep HX (2020) Plant species identification from leaf patterns using histogram of oriented gradients feature space and convolution neural networks. Journal of Information and Telecommunication 4: 140–150.

37. Zeng J, Chen Y, Zhai Y, Gan J, Feng W, Wang F (2019) A Novel Finger-Vein Recognition Based on Quality Assessment and Multi-Scale Histogram of Oriented Gradients Feature. International Journal of Enterprise Information Systems (IJEIS) 15: 100–115.

38. Zhou W, Gao S, Zhang L, Lou X (2020) Histogram of Oriented Gradients Feature Extraction From Raw Bayer Pattern Images. IEEE Transactions on Circuits and Systems II: Express Briefs 67: 946–950.

39. Sokolova M, Japkowicz N, Szpakowicz S. Beyond accuracy, F-score and ROC: a family of discriminant measures for performance evaluation; 2006. Springer. pp. 1015–1021.

40. Tiun S. Experiments on Malay short text classification; 2017. IEEE. pp. 1–4.

41. May RJ, Maier HR, Dandy GC (2010) Data splitting for artificial neural networks using SOM-based stratified sampling. Neural Networks 23: 283–294. https://doi.org/10.1016/j.neunet.2009.11.009 PMID: 19959327

42. Beale MH, Hagan MT, Demuth HB. Neural network toolbox™ user's guide; 2012. Citeseer.

43. Çelik H, Dülger L, Topalbekiroğlu M (2014) Development of a machine vision system: real-time fabric defect detection and classification with neural networks. The Journal of The Textile Institute 105: 575–585.

44. Al-Dhief FT, Latiff NMaA, Malik NNNA, Salim NS, Baki MM, Albadr MAA, et al. (2020) A Survey of Voice Pathology Surveillance Systems Based on Internet of Things and Machine Learning Algorithms. IEEE Access 8: 64514–64533.

45. Khan AI, Shah JL, Bhat MM (2020) Coronet: A deep neural network for detection and diagnosis of COVID-19 from chest x-ray images. Computer Methods and Programs in Biomedicine: 105581. https://doi.org/10.1016/j.cmpb.2020.105581 PMID: 32534344

46. Obaid OI, Mohammed MA, Ghani M, Mostafa A, Taha F (2018) Evaluating the performance of machine learning techniques in the classification of Wisconsin Breast Cancer. International Journal of Engineering & Technology 7: 160–166.

47. Ozturk T, Talo M, Yildirim EA, Baloglu UB, Yildirim O, Acharya UR (2020) Automated detection of COVID-19 cases using deep neural networks with X-ray images. Computers in Biology and Medicine: 103792. https://doi.org/10.1016/j.compbiomed.2020.103792 PMID: 32568675

48. Niu P, Ma Y, Li M, Yan S, Li G (2016) A kind of parameters self-adjusting extreme learning machine. Neural Processing Letters 44: 813–830.

49. Vapnik VN (1999) An overview of statistical learning theory. IEEE transactions on neural networks 10: 988–999. https://doi.org/10.1109/72.788640 PMID: 18252602

50. Nour M, Cömert Z, Polat K (2020) A novel medical diagnosis model for COVID-19 infection detection based on deep features and Bayesian optimization. Applied Soft Computing: 106580. https://doi.org/10.1016/j.asoc.2020.106580 PMID: 32837453

51. Meyer D, Wien FT (2015) Support vector machines. The Interface to libsvm in package e1071 28.

52. Pakyurek M, Atmis M, Kulac S, Uludag U (2020) Extraction of Novel Features Based on Histograms of MFCCs Used in Emotion Classification from Generated Original Speech Dataset. Elektronika ir Elektrotechnika 26: 46–51.

53. Sun Y, Xue B, Zhang M, Yen GG, Lv J (2020) Automatically Designing CNN Architectures Using the Genetic Algorithm for Image Classification. IEEE Transactions on Cybernetics. https://doi.org/10.1109/TCYB.2020.2983860 PMID: 32324588

54. Phung SL, Bouzerdoum A (2009) Matlab library for convolutional neural networks. ICT Research Institute, Visual and Audio Signal Processing Laboratory, University of Wollongong, Tech Rep.

55. Wu J (2017) Introduction to convolutional neural networks. National Key Lab for Novel Software Technology Nanjing University China 5: 23.

56. Abbas A, Abdelsamea MM, Gaber MM (2020) Classification of COVID-19 in chest X-ray images using DeTraC deep convolutional neural network. arXiv preprint arXiv:200313815.

57. Ezzat D, Ella HA (2020) GSA-DenseNet121-COVID-19: a hybrid deep learning architecture for the diagnosis of COVID-19 disease based on gravitational search optimization algorithm. arXiv preprint arXiv:200405084.

58. Hassanien AE, Mahdy LN, Ezzat KA, Elmousalami HH, Ella HA (2020) Automatic x-ray covid-19 lung image classification system based on multi-level thresholding and support vector machine. medRxiv.

59. Hemdan EE-D, Shouman MA, Karar ME (2020) Covidx-net: A framework of deep learning classifiers to diagnose covid-19 in x-ray images. arXiv preprint arXiv:200311055.

60. Maghdid HS, Asaad AT, Ghafoor KZ, Sadiq AS, Khan MK (2020) Diagnosing COVID-19 pneumonia from X-ray and CT images using deep learning and transfer learning algorithms. arXiv preprint arXiv:200400038.